

## **SENSORS/ALGORITHM DEVELOPMENT**

The laboratory's mission enfolds the observations of many components of the hydrological budget. The rising number of satellite sensors for Earth observation presents unique challenges and opportunities for creation and/or refinement of geophysical parameter retrievals techniques. These activities are essential to the success of NASA's Earth science enterprise. One key part of Goddard's contribution to the Earth science community is the design, validation, calibration, and refinement of such techniques. There are twelve papers from the Laboratory that fall under this subtopic for calendar year 2002. The launch of Aqua satellite in May 2002 promises the new observational capability in the infrared and microwave regions, as well as the flow of additional measurements from similar sensors that already existed in Terra satellite; a paper summarizes the instrument suite of this new platform. The MODIS onboard the Terra satellite has been providing measurements of land, ocean and atmospheric parameters since 1999, and a paper gives a timely assessment of the performance of this instrument during its first year of operation. Three papers deal with various aspects of ocean color measurements. The remaining seven papers in the microwave region are related to the studies of noise-level assessment of various orbiting altimeters, the effect ionosphere on L-band sea surface salinity measurements, as well as the retrievals of water vapor, rain parameters, and water surface emissivities. The span of applications is broad and we invite the reader to thumb through these efforts and directly contact authors within the laboratory to discuss findings for future collaborations.

# Is desert dust making oligotrophic waters greener?

H. Claustre,<sup>1</sup> A. Morel,<sup>1</sup> S. B. Hooker,<sup>2</sup> M. Babin,<sup>1</sup> D. Antoine,<sup>1</sup> K. Oubelkheir,<sup>1</sup>  
A. Bricaud,<sup>1</sup> K. Leblanc,<sup>3</sup> B. Quéguiner,<sup>3</sup> and S. Maritorena<sup>4</sup>

Received 8 September 2001; accepted 28 January 2002; published 28 May 2002.

[1] In situ optical measurements provide evidence that oligotrophic waters of the Mediterranean Sea have a greener color than would result from their phytoplankton content alone. This anomaly, detectable in low chlorophyll waters, remains unnoticed in the chlorophyll-rich waters of the nearby waters of the Moroccan upwelling zone. It is due to enhanced absorption in the blue and enhanced backscattering in the green parts of the visible spectrum likely resulting from the presence of submicron Saharan dust in suspension within the upper layer. This result implies that regional estimations of carbon fixation from ocean color images might be significantly overestimated, not only in the Mediterranean Sea, but also in other oligotrophic areas of the Northern hemisphere, subjected to desert dust deposition. **INDEX TERMS:** 4552 Oceanography: Physical: Ocean optics; 4805 Oceanography: Biological and Chemical: Biogeochemical cycles (1615); 1640 Global Change: Remote sensing

## 1. Introduction

[2] Brick-red or pink dust massively exported from the Sahara is at the origin of the so-called "red-rains", sporadically falling over Europe. Besides this spectacular effect, Saharan dust influences several atmospheric and marine processes, such as regional radiative budgets [Legrand *et al.*, 1992], the formation of clouds and rain [Levin and Ganor, 1996], the acidity of rainfall [Løye-Pilot *et al.*, 1986]. Dust deposition also affects sedimentary processes and the biogeochemistry of the Mediterranean Sea, including, perhaps, its productivity through iron enrichment of surface waters [Guerzoni *et al.*, 1997]. Desert dust also impacts optical properties of the atmosphere, leading to some biases in the retrieval of the chlorophyll *a* concentration ( $\langle \text{Chla} \rangle$ ) from color images of the upper ocean [Moulin *et al.*, 2001].

[3] The possible effect of desert dust on optical properties of oceanic waters remains however unknown. Therefore, one of the objectives of the PROSOPE (French acronym for Productivity of Pelagic Oceanic Systems) cruise (Figure 1) was to examine if any peculiar optical characteristic caused by Saharan dust deposition could be detected in oligotrophic Mediterranean waters, that would bias the optical assessment (in situ or remotely) of ( $\text{Chla}$ ).

## 2. Methods-Background

[4] The cruise took place from 4 September to 4 October, 1999. The upwelling waters off Morocco (UPW station) were sampled over 3 days, and the MIO (Ionian Sea, eastern basin) and DYF

(Ligurian Sea, western basin) stations were occupied for 5 days each. Short intermediate stations (St 1 to St 9) were sampled over 4-h periods. Optical measurements and pigment sampling were always performed around noon, within 1 h of overflight by the SeaWiFS satellite.

[5] ( $\text{Chla}$ ) was analysed according to a slightly modified version of the HPLC method described by Vidussi *et al.* [1996]. The accuracy of ( $\text{Chla}$ ) measurements (8%) was checked as part of an international intercomparison exercise (four laboratories were involved) performed on samples taken during the cruise [Hooker *et al.*, 2001].

[6] In situ spectral measurements of upwelling irradiance or radiance and downwelling irradiance were performed using three instruments: LI-1800 LICOR, Satlantic LoCNES and Satlantic SeaFALLS.

[7] The reflectance of a water body,  $R(\lambda)$ , is defined as the ratio of upwelling irradiance (or radiance) to downwelling irradiance, and the spectral shape of  $R(\lambda)$  define the so-called "water color". This color is indexed by the blue-to-green reflectance ratio ( $B/G$ ),  $R(443)/R(555)$ , which, in open-ocean (Case-1) water is essentially governed by the phytoplankton content (actually  $B/G$  decreases with increasing phytoplankton content). Therefore, algorithms have been developed that relate surface ( $\text{Chla}$ ) to  $B/G$  [O'Reilly *et al.*, 1998; Morel and Maritorena, 2001].  $R(\lambda)$  is approximately proportional to the ratio of the backscattering and absorption coefficients,  $b_b(\lambda)/a(\lambda)$ .

## 3. Results

[8] The PROSOPE data set spans two orders of magnitude in surface ( $\text{Chla}$ ) (0.03 to 3.75  $\text{mg m}^{-3}$ ) and about one order of magnitude in  $B/G$  (0.5 to 6.7) (Figure 2). Data collected in the upwelling (station UPW) off Morocco, are in close agreement with global algorithms (Figure 2). This is no longer the case for Mediterranean waters which look systematically greener (lower  $B/G$ ) than typical oceanic waters with the same ( $\text{Chla}$ ), as already observed by Gitelson *et al.* [1996] for the eastern Mediterranean sea. As a consequence, derivation of ( $\text{Chla}$ ) from  $B/G$  measurements through conventional algorithms overestimates actual ( $\text{Chla}$ ) in Mediterranean waters by a factor exceeding 2 (Table 1).

[9] For a given ( $\text{Chla}$ ), a lower than expected  $B/G$  (Figure 2) is due to a lower than expected  $b_b(440)/b_b(555)$  and/or a lower than expected  $a(555)/a(440)$ . When compared to optical properties modeled for a standard ocean with similar ( $\text{Chla}$ ), PROSOPE data show two important features (Table 1): (i) the color shift is caused by both anomalous absorption and backscattering ratios (Mediterranean waters absorb more blue light and backscatter more green light than anticipated); and (ii) the particle scattering coefficients,  $b_b(555)$ , are anomalously high compared to those modeled for a standard ocean.

[10] Additional absorption measurements performed during the cruise permitted an inquiry into the substance(s) potentially responsible for the  $B/G$  changes. An absorption budget can be written as:

$$a(\lambda) = a_w(\lambda) + a_p(\lambda) + a_{os}(\lambda) \quad (1)$$

<sup>1</sup>Laboratoire d'Océanographie de Villefranche, Villefranche-sur-mer, France.

<sup>2</sup>Laboratory for Hydrospheric Processes, NASA Goddard Space Flight Center, Greenbelt, MD, USA.

<sup>3</sup>Laboratoire d'Océanographie et de Biogéochimie, Marseille, France.

<sup>4</sup>Institute for Computational Earth System Science, University of California, Santa Barbara, CA, USA.

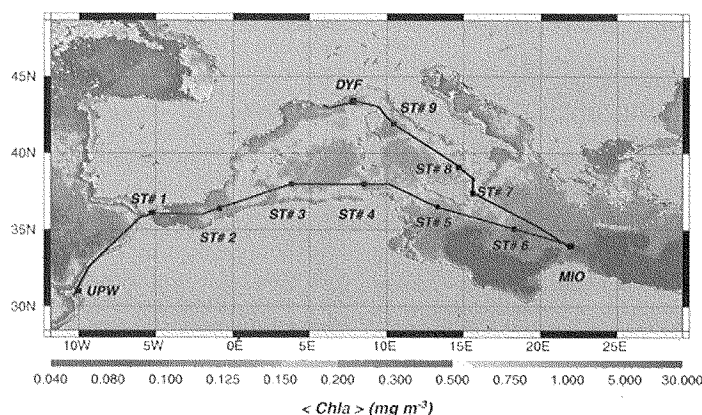


**Figure 1.** PROSOPE cruise track superimposed on the composite SeaWiFS image of surface  $\langle \text{Chla} \rangle$  for September 1999. This composite was derived from SeaWiFS reflectances using the OC4v4 algorithm [O'Reilly *et al.*, 1998].

where  $a(\lambda)$  is the total absorption,  $a_w(\lambda)$  and  $a_p(\lambda)$  are the absorption by water and particles (phytoplankton, heterotrophs, and associated biogenic detritus), respectively and  $a_{OS}(\lambda)$  is a residual term accounting for “other substances”. The latter can be estimated by subtraction, because  $a_w(\lambda)$  is known and  $a(\lambda)$  and  $a_p(\lambda)$  were measured.

[11] The high  $a_p(440)$  values (Table 1) result primarily from the presence of non-photosynthetic carotenoids, typical of algae in oligotrophic surface waters, and, to a lesser extent, from non-algal particles. Such a pigmentation slightly decreases the ratio

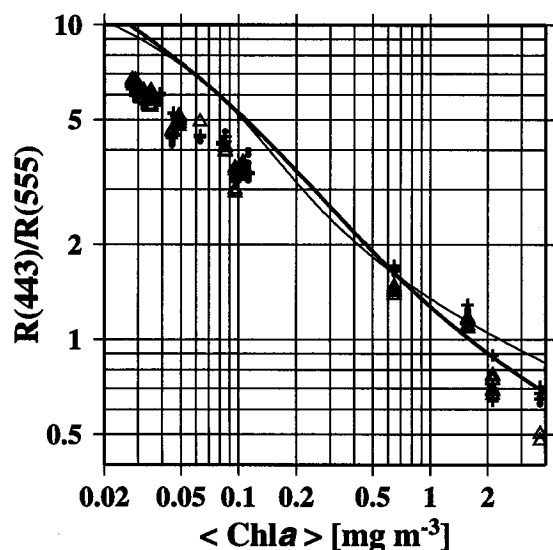


**Figure 2.** Relationship between surface  $\langle \text{Chla} \rangle$  and the blue-to-green reflectance ratio derived from in situ data (determined just below the surface). The  $\langle \text{Chla} \rangle$  values below  $0.15 \text{ mg m}^{-3}$  are from the Mediterranean, and values  $>0.6 \text{ mg m}^{-3}$  are from the upwelling area off Morocco. The blue-to-green reflectance ratios were derived from spectral irradiance or radiance measurements performed by a LI-1800 LICOR ( $\Delta$ ), aSAtlantic LoCNESS ( $\blacktriangle$ ) and aSAtlantic SeaFALLS (+). The field data are compared to an empirical model [O'Reilly *et al.*, 1998] (algorithm OC4v4, thin line) and to a semi-analytical model [Morel and Maritorena, 2001] (thick line).

$a(555)/a(440)$ . In open-ocean Case-1 waters,  $a_{OS}$  is generally believed to result from the presence of colored dissolved organic matter (CDOM). However, the PROSOPE  $a_{OS}(440)$  values are inappropriately high when compared to modeled  $a_{CDOM}(440)$  values for standard oceanic waters. Moreover, high CDOM content is unlikely for two reasons: (i) CDOM is a by-product of biological activity, which is rather low in the Mediterranean; and (ii) CDOM is exposed to intense photo-bleaching [Vodacek *et al.*, 1997], favored by the summer vertical stratification combined with high surface irradiance. In addition, CDOM has no scattering capability able to account for the high  $b_p(555)$  value as well as for the unexpectedly low  $b_b(440)/b_b(555)$  ratio, also observed. The presence of bubbles could be put forward to account for the enhanced scattering coefficient [Zhang *et al.*, 1998]. It is unlikely, however, as the conditions during the cruise were exceptionally good in term of sea state and ambient wind.

[12] Given that algal, non-algal particles, CDOM and bubbles are not plausible causes for concomitant decreases in both  $a(555)/a(440)$  and  $b_b(440)/b_b(555)$ , and for enhanced  $b_p(555)$  values, “other substances” have to be found to explain the conspicuous green color shift. We suggest that submicron Saharan dust, probably smaller than  $0.7 \mu\text{m}$  [D’Almeida, and Schütz, 1983; Gomes *et al.*, 1990], is responsible for this unexpected observation.

## 5. Concluding Remarks

[17] It has been shown that the presence of non-phytoplankton constituents — namely of dust — in open ocean waters with low  $\langle \text{Chla} \rangle$  can depress the in situ B/G compared to its expected value. Moreover, the remotely-sensed B/G can be even more lowered because the atmospheric correction of the blue bands is less accurate when absorbing aerosols are present in the atmosphere [Moulin *et al.*, 2001], which leads to an underevaluation of the actual B/G. This appears to be the case in oligotrophic Mediterranean waters where the  $\langle \text{Chla} \rangle$  retrieved from SeaWiFS (Figure 1) are distinctly higher than the sea truth data (Table 1). These observations suggest that regional algorithms are needed and that the dependence of  $\langle \text{Chla} \rangle$  retrieval on the proximity of desert dust sources must be systematically investigated. Given the large spatial extension of sub-tropical gyres, a proper estimation of their contribution to oceanic carbon fixation requires very accurate estimate of their surface  $\langle \text{Chla} \rangle$ . A careful re-examination of their optical properties is, therefore, a prerequisite to address (and quantify) potential dust-induced bias in  $\langle \text{Chla} \rangle$  retrieval.

# On-orbit performance of the Earth Observing System Moderate Resolution Imaging Spectroradiometer; first year of data

B. Guenther<sup>a,\*</sup>, X. Xiong<sup>b</sup>, V.V. Salomonson<sup>a</sup>, W.L. Barnes<sup>a</sup>, James Young<sup>c</sup>

<sup>a</sup>NASA's Goddard Space Flight Center, Greenbelt, MD 20771, USA

<sup>b</sup>Science Systems Applications, Inc., Suite 104, 7501 Forbes Boulevard, Seabrook, MD 20706, USA

<sup>c</sup>Raytheon, Santa Barbara Remote Sensing, Building 32, 75 Coromar Drive, Goleta, CA 93117, USA

Received 5 April 2001; received in revised form 31 January 2002; accepted 1 March 2002

## Abstract

The Moderate Resolution Imaging Spectroradiometer (MODIS) completed the first year of science data acquisition on February 24, 2000. The overall performance of the sensor and the on-board calibration systems for this first year have been very good. Several features of the performance lead to characteristics in the data set that merit special attention. These items are sometimes called data product caveats, and are described here. Uncertainty budgets for the 0.555- $\mu\text{m}$  band, the 1.240- $\mu\text{m}$  band and the 12.000- $\mu\text{m}$  band are presented at several days throughout this first year. The uncertainty is estimated to be decreasing with time during this period, and to be near 1.8% in reflectance factor for 0.555  $\mu\text{m}$ , 1.9% for the reflectance factor product for the 1.240  $\mu\text{m}$  band, and 0.7% for the 12.000- $\mu\text{m}$  band at nadir at the end of the first year. Degradation of the solar diffuser is 2.3% at 0.412  $\mu\text{m}$ , known to an uncertainty of  $\pm 0.5\%$ . Solar diffuser degradation for wavelengths longer than 0.5  $\mu\text{m}$  is indistinguishable from the uncertainty in trend determination for the first year. Mirror side degradation at 0.412  $\mu\text{m}$  is  $6 \pm 0.5\%$ , with a mirror side difference of an additional 3%. The performance present in the data at the end of year 1 provides significant encouragement that many improvements in our understanding of the Earth system performance can and will be based on MODIS data during the coming years.

© 2002 Published by Elsevier Science Inc.

## 1. Introduction

The Earth Observing System (EOS) was designed to provide observations that would enable better understanding on a global scale of the entire Earth system and the included processes. There was and there is urgency attached to this effort because an expanding human population is more affected by natural variability in the environment and, more importantly, has become an active participant in the evolution of the Earth system. To address questions that were both scientifically important, and relevant to resource management and sustainability policies, many sensors were designed with considerable attention to enhancing existing data bases for cloudiness, sea surface temperature, land cover, etc. Key among these sensors is the Moderate Resolution Imaging Spectroradiometer (MODIS) whose heritage comes from the NOAA Advanced High Resolution Radiometer (AVHRR), the Nimbus Coastal Zone Color Scanner (CZCS) and the Orbview-2 SeaWIFS sensor, the NOAA High-resolution Infrared Sounder (HIRS), and the Landsat Thematic Mapper. MODIS has been designed as a primary sensor to address questions related to: atmospheric

variables such as cloud properties, radiative fluxes, and aerosol properties; land variables such as land cover and land use change, vegetation dynamics, surface temperature, fire occurrence, volcanic effects, and snow cover and, ocean variables such as sea surface temperature, and ocean color related to phytoplankton distribution and dynamics and photosynthetic efficiency.

MODIS was launched on the EOS Terra spacecraft on 18 December 1999. Initial engineering data was returned almost immediately, and science data was acquired first on 24 February 2000. The MODIS sensor has wide spectral range and wide spatial coverage, with 36 carefully selected bands to observe land, ocean, and atmosphere features on a global basis every 1–2 days (Table 1). The bands are distributed on four local plane assemblies (FPA), with wavelengths between 0.4 and 0.6  $\mu\text{m}$  on the VIS FPA, 0.6–1.0  $\mu\text{m}$  on the NIR FPA, 1.0–5.0  $\mu\text{m}$  on the SW/MWIR FPA and 5.0–15.0  $\mu\text{m}$  on the LWIR FPA. The MODIS measurements program is designed to provide a data set from which scientists can construct models of the Earth's global dynamics—atmospheric, oceanic and terrestrial—and predict changes. Characteristics of the MODIS are described

in Barnes, Pagano, and Salomonson (1998), and its pre-launch calibration is summarized in Guenther, Godden, Xiong, et al. (1998). The purpose of this paper is to summarize the MODIS first year performance in orbit and the resulting quality of the data.

The MODIS includes several calibration systems to provide on-orbit calibration. The early on-orbit performance of these calibration and characterization systems is provided in Section 2. The overall MODIS performance is described

in Section 3. The uncertainty of the resulting radiometrically calibrated data product (Level 1B) is summarized for three bands, with the contributions of several known sensor features highlighted in that analysis. The detailed MODIS performance is described in Section 4. Actions taken to improve performance or better characterize the performance are highlighted, and cautions on how these features may be impacting the Level 1 data set are reviewed as well.

Table 1

Overall characteristics of the MODIS instrument and selected operational specifications

Primary use	Band	Bandwidth <sup>a</sup>	Special radiance <sup>b</sup>	Required SNR <sup>c</sup>	Primary use	Band	Bandwidth <sup>a</sup>	Spectral radiance <sup>b</sup>	Required NEΔT (K) <sup>d</sup>
Land/cloud/	1	620–670	21.8	128	Surface/cloud	20	3.660–3.840	0.45 (300 K)	0.05
aerosols boundaries	2	841–876	24.7	201	temperature	21	3.929–3.989	2.38 (335 K)	2
Land/cloud/	3	459–479	35.3	243		22	3.929–3.989	0.67 (300 K)	0.07
aerosols properties	4	545–565	29	228		23	4.020–4.080	0.79 (300 K)	0.07
	5	1230–1250	5.4	74	Atmospheric	24	4.433–4.498	0.17 (250 K)	0.25
	6	1628–1652	7.3	275	temperature	25	4.482–4.549	0.59 (275 K)	0.25
	7	2105–2155	1	110	Cirrus clouds	26	1.360–1.390	6	150 <sup>c</sup>
Ocean color/	8	405–420	44.9	880	water vapor	27	6.535–6.895	1.16 (240 K)	0.25
Phytoplankton/	9	438–448	41.9	838		28	7.175–7.475	2.18 (250 K)	0.25
Biogeochemistry	10	483–493	32.1	802	Cloud properties	29	8.400–8.700	9.58 (300 K)	0.05
	11	526–536	27.9	754	Ozone	30	9.580–9.880	3.69 (250 K)	0.25
	12	546–556	21	750	Surface/cloud	31	10.780–11.280	9.55 (300 K)	0.05
	13	662–672	9.5	910	temperature	32	11.770–12.270	8.94 (300 K)	0.05
	14	673–683	8.7	1087	Cloud top altitude	33	13.185–13.485	4.52 (260 K)	0.25
	15	743–753	10.2	586		34	13.485–13.785	3.76 (250 K)	0.25
	16	862–877	6.2	516		35	13.785–14.085	3.11 (240 K)	0.25
Atmospheric	17	890–920	10	167		36	14.085–14.385	2.08 (220 K)	0.35
water vapor	18	931–941	3.6	57					
	19	915–965	15	250					

## MODIS Technical Specifications

Orbit: 705 km, 10:30 a.m. descending node (Terra) or 1:30 p.m. ascending node (Aqua), sun synchronous, near-polar, circular.

Scan rate: 20.3 rpm, cross-track.

Swath dimensions: 2330 km (cross-track) by 10 km (along track at nadir).

Telescope: 17.78 cm diameter off-axis, afocal (collimated), with intermediate field stop.

Size: 1.0 × 1.6 × 1.0 m.

Weight: 228.7 kg.

Power: 162.5 W (single orbit average).

Data rate: 10.6 Mbps (peak daytime); 6.1 Mbps (orbital average).

Quantization: 12 bits.

Spatial resolution: 250 m (Bands 1–2); 500 m (Bands 3–7); 1000 m (Bands 8–36).

Design life: 6 years.

<sup>a</sup> Bands 1–19 are in nm; Bands 20–36 are in μm.<sup>b</sup> Special radiance values are (W/m<sup>2</sup> μm sr).<sup>c</sup> SNR = signal-to-noise ratio.<sup>d</sup> NEΔT = noise-equivalent temperature difference.

## 5. Summary and conclusions

The completion of the first year of MODIS operations has demonstrated that the derived data products will enable significant improvements in our understanding of the Earth systems. Data sets for annual and longer-term performance likely will start near 1 November 2000. The noise charts presented in Section 3 indicate that the sensor is capable of low noise measurements at nearly all wavelengths. The sample uncertainty tables indicate that the Level 1 calibration products are expected to meet the very demanding uncertainty measurements under many geophysical conditions. On the other hand, Section 4 provides a list of areas where initial MODIS performance was different than

expected, and where significant improvements were needed to allow the derived data to meet scientific expectations. Numerous improvements now are in place. Continued improvements are being sought for even better quality MODIS data. The documentation for these improvements is available from the MODIS and MCST web pages. MODIS may be the most complex instrument built and flown on a spacecraft for civilian research purposes, and the performance present in the data at the end of year 1 provides significant encouragement that many improvements in our understanding of the Earth system performance can and will be based on MODIS data during the coming years.

# An Evaluation of Above- and In-Water Methods for Determining Water-Leaving Radiances

STANFORD B. HOOKER

*NASA Goddard Space Flight Center, Greenbelt, Maryland*

GORDANA LAZIN

*Satlantic, Inc., Halifax, Nova Scotia, Canada*

GIUSEPPE ZIBORDI

*Joint Research Centre, Ispra, Italy*

SCOTT MCLEAN

*Satlantic, Inc., Halifax, Nova Scotia, Canada*

(Manuscript received 30 August 2000, in final form 17 August 2001)

## ABSTRACT

A high-quality dataset collected at an oceanographic tower was used to compare water-leaving radiances derived from simultaneous above- and in-water optical measurements. The former involved two different above-water systems and four different surface glint correction methods, while the latter used three different in-water sampling systems and three different methods (one system made measurements a fixed distance from the tower, 7.5 m; another at variable distances up to 29 m away; and the third was a buoy sited 50 m away). Instruments with a common calibration history were used, and to separate differences in methods from changes in instrument performance, the stability (at the 1% level) and intercalibration of the instruments (at the 2%–3% level) was performed in the field with a second generation Sea-viewing Wide Field-of-view Sensor (SeaWiFS) Quality Monitor (SQM-II). The water-leaving radiances estimated from the methods were compared to establish their performance during the field campaign, which included clear and overcast skies, Case-1 and Case-2 conditions, calm and roughened sea surface, etc. Three different analytical approaches, based on unbiased percent differences (UPDs) between the methods, were used to compare the various methods. The first used spectral averages across the 412–555-nm SeaWiFS bands (the part of the spectrum used for ocean color algorithms), the second used the ratio of the 490- and 555-nm bands, and the third used the individual (discrete) wavelengths. There were eight primary conclusions of the comparisons, which were considered within the context of the SeaWiFS 5% radiometric objectives. 1) The 5% radiometric objective was achieved for some in-water methods in Case-1 waters for all analytical approaches. 2) The 5% radiometric objective was achieved for some above-water methods in Case-2 waters for all analytical approaches, and achieved in both water types for band ratios and some discrete wavelengths. 3) The largest uncertainties were in the blue domain (412 and 443 nm). 4) A best-to-worst ranking of the in-water methods based on minimal comparison differences did not depend on the analytical approach, but a similar ranking of the above-water methods did. 5) Above- and in-water methods not specifically designed for Case-2 conditions were capable of results in keeping with those formulated for the Case-2 environment or in keeping with results achieved in Case-1 waters. 6) There was a significant difference between two above-water instruments oriented perpendicular with respect to the sun, but pointed in the same direction (best agreement) versus the opposite direction (worst agreement). 7) The overall intercomparison of all methods across Case-1 and Case-2 conditions was at the 9.1% level for the spectral averages, and at the 3.1% level for the band ratios (uncertainties other than those associated with implementing the individual methods account for 2%–4% and 1%–3% of these values, respectively). 8) A comparison with traditional regression analyses confirms the UPD conclusions.

## 1. Introduction and background

Spectral water-leaving radiance,  $L_w(\lambda)$ , is the central physical quantity for bio-optical studies in the upper ocean; whether determined from above- or in-water data,  $\hat{L}_w(\lambda)$  and  $\tilde{L}_w(\lambda)$ , respectively, it must be accurately measured. The Sea-viewing Wide Field-of-view Sensor (SeaWiFS) Project, for example, requires  $L_w(\lambda)$  uncertainties within 5% (Hooker et al. 1993b). This was shown to be achievable for in-water measurements in Case-1 waters using primarily a single methodology (Hooker and Maritorena 2000), but the uncertainty associated with multiple methods has not been well quantified. The SeaWiFS calibration and validation plan (Hooker and McClain 2000) has emphasized in-water field work because when the plan was conceived, the above-water protocols were not as mature as the in-

water protocols (Mueller and Austin 1992). Although there has been steady progress in defining the proper metrology for above-water measurements, intracomparisons within a group of accepted techniques have not occurred. More importantly, intercomparisons between above- and in-water methods have also not been thoroughly investigated, although individual comparisons are available in the literature (e.g., Pinkerton et al. 1999; Toole et al. 2000).

## 6. Conclusions

This study used data from three different environmental conditions that covered much of the dynamic range of in situ optical measurements, but, nonetheless, it was based on a small dataset collected during three



days of measurements in the near-coastal environment. One of the three days (SDY 194) was within the parameter range established by the NRSR Workshop; the other two were not, but they were typical of the kinds of environmental conditions that can be encountered during above- and in-water radiometric field campaigns. Three in-water methods for determining water-leaving radiances from profiling (S84) and fixed-depth (P94 and P97) sampling systems were combined with four above-water methods to quantify the performance of all the methods. The removal of glint contamination from the surface measurement distinguished the above-water methods from one another and included four correction schemes: near-infrared radiance ratio (M80), Fresnel reflectance plus residual reflection (C85), modified Fresnel reflectance (S95), and near-infrared irradiance ratio (L98).

The seven methods, three different days of environmental conditions, and five sampling platforms produced a large number of performance comparisons, which were separated according to UPD analyses based on spectral averages, band ratios, and discrete wavelengths. Although each method was usually found superior to the others at some stage in the performance evaluation process, the most suitable point for overall evaluation is at the intercomparison level summarized in Tables 6–9 and Figs. 8–9. Based on these summaries, some general capabilities concerning all the methods can be discerned.

- 1) In terms of the 5% calibration and validation objective, and the hoped for performance to within 3%, the spectral-average approach (Table 7d) produced larger average differences (and standard deviations) than the band-ratio approach (Table 8d), which were 9.1% (5.6%) and 3.7% (1.1%), respectively. Using band ratios, the S84, P94, C85, and S95 methods produced ranges of expected differences (average plus and minus 1 standard deviation) within the 5% level, and frequently to within 3%.
- 2) The best results were not restricted to Case-1 or clear-sky conditions; water type was seen to be important, although other environmental parameters agreed well with the UPD levels (considered in more detail below). Consider, for example, the difficult circumstance of overcast conditions, which can be highly variable in terms of sky radiance distribution and relative (percent) variations in illumination conditions during a deployment interval. Because of the low signal levels, small absolute differences represent large relative discrepancies, but all the methods agreed very well for overcast conditions when using the data from the same instrument.
- 3) Above- and in-water methods not formulated for Case-2 conditions were capable of results in keeping with those achieved in Case-1 waters (e.g., Table 6). Agreement to within 5% was achieved with in-water methods in Case-1 waters for all three analytical approaches. Agreement within 5% was achieved with above-water methods in Case-2 waters for all analytical approaches, and was achieved in both water types for the band-ratio and discrete wavelength

analyses (spectral averages were elevated due to large uncertainties in the blue domain).

- 4) For both above- and in-water methods, the largest uncertainties were usually associated with the blue part of the spectrum (412–443 nm), with the blue-green transition (490–510 nm) a local minimum, which was followed by a small increase at 555 nm (Table 9). The above-water methods that calculated the surface reflectance by assuming  $\lambda_r = 0$  (M80 and L98) were spectrally dependent during Case-2, clear-sky conditions, with very large uncertainties at 412 nm (as much as 38%) and minimum uncertainties at 555 nm (less than 5%).

Note that all of the analytical approaches yielded average uncertainties across all three days and all methods below the 10% level, so for applications where this level of agreement is acceptable—for example, perhaps with large-scale bio-optical models, any of the methods are probably acceptable. It is also important to remember the regression analysis results confirm these overall conclusions (although there are small shifts in the magnitude of the uncertainties).

For the in-water methods alone, the specific details of the capabilities of the methods are as follows.

- 5) P94 and P97 grouped together, but S84 performed the best. Consequently, an in-water method making use of vertical profiles of the water column should be considered superior than those using sensors at a fixed depth, although good results were obtained for the latter during Case-1 conditions and for band-ratio analyses.
- 6) The best-to-worst ranking of the in-water methods (using the minimal range in average differences) did not depend on the analytical approach (S84, P94, and P97), but the ranking of the above-water methods did (S95, L98, C85, and M80 for the spectrally averaged approach; and C85, S95, M80, and L98 for the band-ratio approach).
- 7) The in-water spectral averages intracompared best during Case-1 conditions and worst during Case-2 conditions (Table 7c), which is consistent with the higher variability associated with the latter; however, the opposite result was seen with the band-ratio analysis (Table 8c).

Before considering the above-water methods separately, it is important to remember proper data filtering to remove glint spikes is an essential part of above-water methods that permit it (the C85 method does not). Although many schemes were considered in this study (section 3c), the adopted filter retained only the lowest 5% of the data, based on the reddest (780-nm) band. Similarly, data averaging was shown to needlessly and significantly degrade the quality of the above-water data because it artificially elevated the  $L_T(\lambda)$  values by contaminating them with glint. Subsampling did not degrade the above-water data as significantly as averaging, but it showed that above-water sampling rates should be equal to, or greater than, 1 Hz (Fig. 7). The conclusion to be derived here is the glint field must be adequately discretized, so it can be removed by filtering.

# The Effect of the Ionosphere on Remote Sensing of Sea Surface Salinity From Space: Absorption and Emission at L Band

David M. Le Vine, *Fellow, IEEE*, and Saji Abraham, *Member, IEEE*

**Abstract**—The purpose of this work is to examine the effects of Faraday rotation and attenuation/emission in the ionosphere in the context of a future remote sensing system in space to measure salinity. Sea surface salinity is important for understanding ocean circulation and for modeling energy exchange with the atmosphere. A passive microwave sensor in space operating near 1.4 GHz (L-band) could provide global coverage and complement in situ arrays being planned to provide subsurface profiles. However, the salinity signal is relatively small and changes along the propagation path can be important sources of error. It is shown that errors due to the ionosphere can be as large as several psu. The dominant source of error is Faraday rotation but emission can be important.

**Index Terms**—Ionospheric electromagnetic propagation, microwave radiometry, ocean salinity, remote sensing.

## I. INTRODUCTION

THE SALINITY of the open ocean is important for understanding ocean circulation and for modeling energy exchange with the atmosphere. For example, salinity gradients affect mixed layer processes, which influence fluxes of heat near the surface [1]. Salinity and temperature determine water density and are important factors in large-scale ocean circulation [2]. Also, changes in salinity are primarily caused by changes in freshwater (evaporation, precipitation, melting ice, or river input). These changes are manifestations of elements of the water cycle, which are poorly known over the ocean [3].

Microwave remote sensing from space could provide the necessary temporal and spatial sampling needed to understand the role of salinity in these ocean processes [2], [4]. Changes in salinity modulate the emissivity of the surface and cause changes in emission that are sufficiently strong in the low frequency portion of the microwave spectrum to be detected with passive sensors [5], [6]. Measurements from space have been proposed [7] and salinity differences were observed from space with the L-band radiometer on SKYLAB 25 [8]. Recently, experiments with L-band radiometers on aircraft have demonstrated that salinity can be retrieved with accuracy useful for studying processes in coastal regions [9], [10].

However, measurement of sea surface salinity (SSS) in the open ocean presents a special challenge. This is so because the dynamic range of SSS in the open ocean is relatively small (about 5 K) and the requirements for a scientifically useful measurement (about 0.05 K) put a severe constraint on radiometric performance. A change of 0.05 K at L-band corresponds to a change of about 0.1 psu [7] where “psu” denotes changes measured on the practical salinity scale [11]. To put the challenge of this measurement in perspective, the dynamic range associated with changes in soil moisture is on the order of 100 K [12] and measurement requirements are 1–4 K [13].

Among the important potential sources of error at L-band is the ionosphere. The ionosphere causes a change in the direction of polarization (Faraday rotation) and because the ionosphere is lossy at L-band, there is both attenuation and emission along the signal path. As will be shown here, both phenomena can cause errors that are important for remote sensing of salinity at the 0.1-psu level of accuracy. A brief background is given in Appendices A and B to define Faraday rotation and attenuation in the ionosphere. In Section II, the magnitude of Faraday rotation and its effect on observed brightness temperature are presented. In Sections III–IV, attenuation and its effect on brightness temperature (emission) are discussed.

## II. FARADAY ROTATION

### A. Magnitude

The rotation of the polarization vector in the ionosphere is due to the change along the propagation path from surface to sensor of the phase,  $\Omega$ , in (B3). Substituting (A6) into (B4) and integrating along the propagation path,  $s$ , one obtains

$$\Omega_F = \left( \frac{\pi}{c\nu^2} \right) \int \nu_p^2(s) \nu_B(s) \cos(\Theta_B(s)) ds \quad (1)$$

where  $\Omega_F$  is the Faraday rotation in radians and  $\Theta_B$  is the angle between the direction of propagation and the Earth magnetic field [14], [15]. To simplify the many calculations needed to make a global map of  $\Omega_F$ , (1) has been approximated by making the change of variables  $ds = \sec(\theta)dz$  where  $z$  is the normal to the surface at the subsatellite point nadir and  $\theta$  is the polar angle between nadir and the line of sight to the surface (incidence angle). Substituting for the plasma frequency,  $\nu_p$  and electron gyro frequency,  $\nu_B$ , from (A2)–(A3) and replacing  $B$  by its value at an altitude of 400 km [16], one obtains

$$\Omega_F \approx 6950 B(400) \cos(\Theta_B) \sec(\theta) \text{VTEC}. \quad (2)$$

Manuscript received June 1, 2001; revised December 13, 2001.

D. M. Le Vine is with the Microwave Sensors Branch/Code 975, Laboratory for Hydrospheric Processes, Goddard Space Flight Center, Greenbelt, MD 20771 USA (e-mail: dmlevine@priam.gsfc.nasa.gov).

S. Abraham is with the Science System and Applications, Inc., Microwave Sensors Branch/Code 975, Goddard Space Flight Center, Greenbelt, MD 20771 USA (e-mail: sabraham@synth.gsfc.nasa.gov).

Publisher Item Identifier S 0196-2892(02)04604-1.



These approximations are reasonable because  $B$  is slowly varying with altitude and because there is little curvature of the ray path. In (2),  $B$  is in tesla,  $\Omega_F$  is in degrees, and  $\text{VTEC} = \int N_e(z)dz$  is the vertical total electron content at the sub-satellite point in total electron content units ( $10^{16}$  electrons/m<sup>2</sup>).

It is clear from (1) and (2) that Faraday rotation depends on electron density and magnetic field and also on the orientation of the sensor with respect to the local magnetic field (i.e., on  $\Theta_B$ ). Examples of the effect of sensor orientation (scan pattern and look angle) can be found in [16]. For purposes of this paper, it will be assumed that the sensor looks to the right (i.e., across track in the plane perpendicular to the satellite heading). The sensor will be assumed to be in a sun-synchronous orbit with an altitude of 675 km, which is representative of orbits proposed for microwave remote sensing at L-band [4]. Faraday rotation will be computed using the International Reference Ionosphere (IRI-95) [17] to generate the necessary electron density profiles and the International Geomagnetic Reference Field (IGRF) [18] for the magnetic field.

## V. COMMENTS

Calculations have been presented here illustrating the effect of Faraday rotation and attenuation/emission from the ionosphere on passive microwave remote sensing at L-band (1.4 GHz). The motivation for this work is current interest in remote sensing of ocean salinity from space. To put the effects of the ionosphere into context, the change of brightness temperature with salinity is about 0.5 K/psu. It is clear from Figs. 2 and 3 (error due to Faraday rotation) and Tables II and III (error due to attenuation and emission) that corrections for these phenomena will have to be made to achieve salinity retrievals accurate to 0.1–0.2 psu.

The data also indicate some obvious choices for remote sensing. Clearly an optimum choice as far as minimizing errors is 6 am local time and as close to a minimum of solar activity as possible. Local time of 6 am is near the minimum in the daily cycle of the ionosphere, (Fig. 7 is an example of the diurnal variation). Remote sensing from a sun-synchronous orbit with an equatorial crossing time of 6am/6pm would provide observations near this minimum. Fig. 1 and Tables I–III illustrate the dependence on solar activity. For a fixed local time and location, Faraday rotation and emission/absorption increase roughly linearly with the solar activity (IG) index,  $R_z$ .

The studies presented here use the IRI-95 and are therefore representative of climatological data for the ionosphere. The IRI-95 model [17] is a good representation of mean characteristics of the ionosphere but is not a particularly good predictor of current (instantaneous) behavior [24], [25]. It may be possible to improve its ability to predict current behavior given input of local, measured parameters [26], [27]. However, without such input corrections for Faraday rotation and emission will likely have to be based on other models or techniques. (One possibility is to measure the third Stokes parameter [28].)

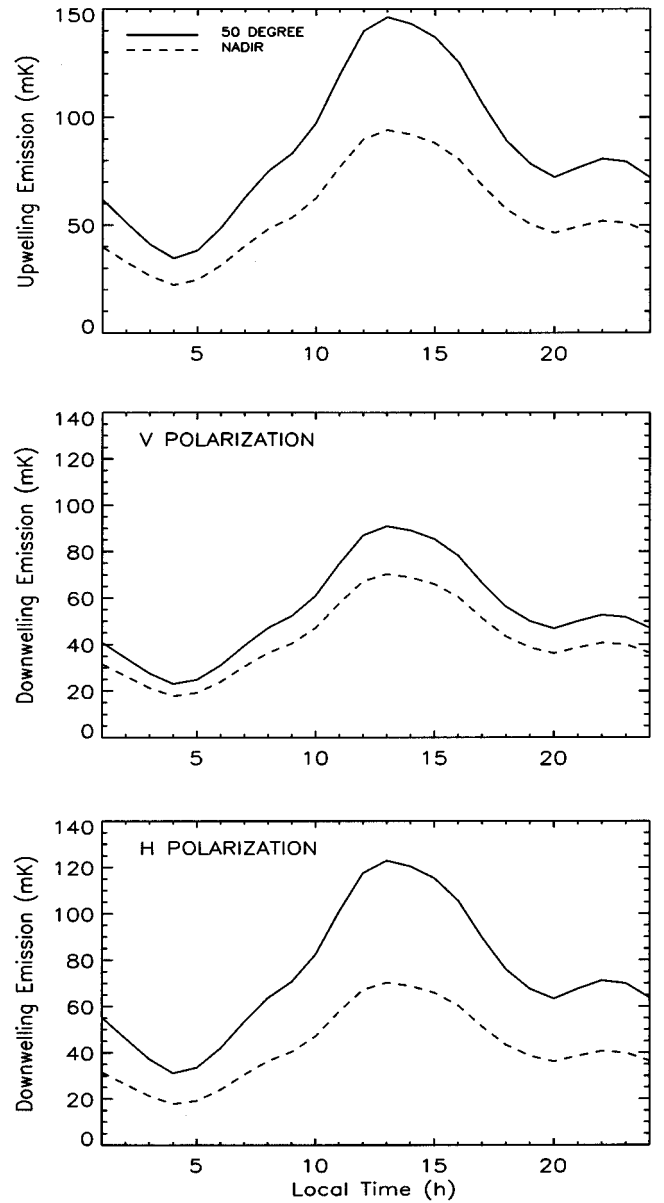


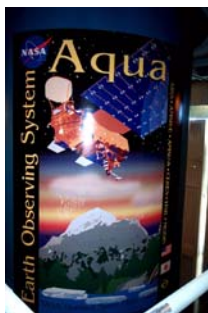
Fig. 7. Diurnal variation of upwelling (top) and downwelling emissions (vertical polarization, middle; horizontal polarization, bottom). The calculations are at 30°N, 330°E during high solar activity (June 1989). The surface is ocean with  $S = 35$  psu and  $T_0 = 20$  °C.

Attenuation is proportional to  $\nu_z$  as in (7) which follows from the Appleton–Hartree equation and simplifications for L-band. This is a “cold” plasma approximation. In the present study, the collision frequency is taken as  $\nu_z = \nu_{\text{eff}}$  (see (9)–(10)). It has been suggested that, when  $\nu \gg \nu_{\text{eff}}$ , as is the case at L-band, a better approximation is to use  $\nu_z = 1.333 \nu_{\text{eff}}$  [29]. Hence, it is likely that the values for emission and loss given here are underestimated. Also, the results presented here employ approximations that are reasonable at low and middle latitudes. Near the poles, additional care must be taken in the calculation of attenuation [30].

# *AQUA: IN ORBIT AND READY FOR THE SCIENTISTS*

Claire L. Parkinson  
NASA Goddard Space Flight Center

After over a decade of development, the Aqua spacecraft was finally launched on May 4, 2002, from Vandenberg Air Force Base in California.



Dozens of Code 400 personnel were critical to its success; and now, as many of them move on to other projects, the core of the Aqua work passes to mission operations, data handlers, and scientists. This article presents an overview of the Aqua mission from the science perspective, emphasizing the Earth-observing instruments and science teams to the exclusion of the equally fascinating and numerous additional aspects of the mission.

Aqua carries six distinct Earth-observing instruments, all placed on board the spacecraft in order to help scientists examine and further understand the Earth's global climate system. As the name suggests, the Aqua mission has a particular concentration on water, with Aqua scientists examining ocean surface water, evaporation from the oceans, water vapor in



**Launch of the Aqua spacecraft, May 4, 2002.**  
(Photo by Bill Ingalls/NASA.)

the atmosphere, clouds, precipitation, soil moisture, snow cover and glacial ice on land, and sea ice in the oceans. In addition to water in all its forms, scientists are also analyzing Aqua data for information on vegetation, ocean productivity, trace gases and aerosols in the atmosphere, and other elements of the Earth's climate system.

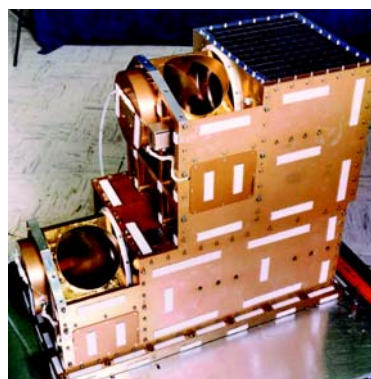
## AIRS/AMSU/HSB



**AIRS. (Photo courtesy of BAE Systems.)**

Of the six Aqua instruments, the one with the greatest technological advances made as part of the Aqua program is the Atmospheric Infrared

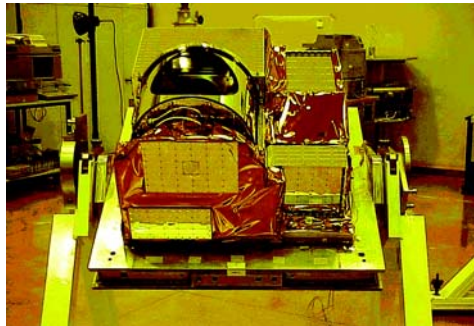
Sounder (AIRS). AIRS is a high-resolution sounder with 2378 channels measuring infrared radiation at wavelengths in the range 3.74-15.4  $\mu\text{m}$  and four channels measuring visible/near-infrared radiation at wavelengths in the range 0.4-1.1  $\mu\text{m}$ .



**AMSU-A1. (Photo courtesy of Aerojet.)**

AIRS is joined on Aqua by two microwave sounders: a 15-channel Advanced Microwave Sounding Unit (AMSU, consisting of two separate units, AMSU-A1 and AMSU-A2) and a four-channel Humidity Sounder for Brazil (HSB), provided by the Instituto Nacional de Pesquisas Espaciais (INPE), the Brazilian National Institute for Space Research. The AMSU and HSB are similar to instruments flying on satellites of the National Oceanic and Atmospheric Administration (NOAA) since May 1998, but when linked with the AIRS on Aqua, they become vital components of the most advanced sounding system ever flown in space: Aqua's AIRS/AMSU/HSB triplet.

The central purpose of the AIRS/AMSU/HSB



**HSB. (Photo courtesy of Brazil's Instituto Nacional de Pesquisas Espaciais.)**

combination is to obtain accurate atmospheric temperatures and humidities throughout the atmosphere, from the surface upward

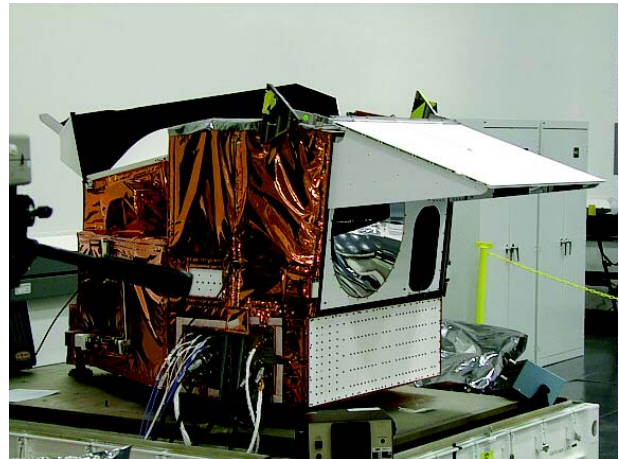
to an altitude of 40 km

## MODIS

The other three instruments on Aqua, outside of the AIRS/AMSU/HSB sounding suite, are the Moderate Resolution Imaging Spectroradiometer (MODIS), the Clouds and the Earth's Radiant Energy System (CERES), and the Advanced Microwave Scanning Radiometer for EOS (AMSR-E). MODIS and CERES instruments are also on Terra, launched in December 1999, and are provided by NASA, while AMSR-E is new and is provided by Japan's National Space Development Agency (NASDA).

## Early Data

All six Earth-observing instruments on Aqua (or seven, when counting the two CERES individually) are now operating and sending down high quality data. The first instrument to be turned on was the



**MODIS. (Photo courtesy of Raytheon.)**

AMSU, on May 12, followed two days later by the HSB. Within days, the AIRS/AMSU/HSB science team had created first-light images from these data streams, mapping color-coded brightness temperatures (reflecting the radiation values received) for individual channels of data across the eastern U.S., the western U.S., and, for the HSB, Brazil. The next instrument to be turned on was NASDA's AMSR-E, with its data flow beginning on May 24. Some initial complications with the AMSR-E data were quickly solved by NASDA, who by June 1 had adjusted the automatic gain control (AGC), correcting the data flow. Days later NASDA created two global maps illustrative of the high quality data from the AMSR-E instrument, one map showing sea surface temperatures and the other showing a color-composite produced from three of the AMSR-E channels.

The AIRS visible data started flowing on May 26, and the AIRS infrared data started to flow on June 12. The CERES data started to flow on June 18, and the MODIS data started on June 24. In each case, very quickly after the instrument was turned on, the relevant science team had created first-light images illustrating the fact that the instrument is working and is obtaining high quality data. The MODIS team has indicated the clearly superior quality of the initial Aqua images versus the initial MODIS images from Terra, where there was an undesired striping; and the AIRS team, in addition to creating images, has plotted infrared spectra at individual points, establishing that every one of the 2378 infrared channels on AIRS is working.

## Assessment of the Cycle-to-Cycle Noise Level of the Geosat Follow-On, TOPEX, and Poseidon Altimeters

N. TRAN

*Raytheon ITSS and NASA Goddard Space Flight Center/Wallops Flight Facility, Wallops Island, Virginia*

D. W. HANCOCK III AND G. S. HAYNE

*NASA Goddard Space Flight Center/Wallops Flight Facility, Wallops Island, Virginia*

D. W. LOCKWOOD

*Raytheon ITSS and NASA Goddard Space Flight Center/Wallops Flight Facility, Wallops, Virginia*

D. VANDEMARK

*NASA Goddard Space Flight Center/Wallops Flight Facility, Wallops, Virginia*

M. L. DRISCOLL AND R. V. SAILOR

*TASC, Inc., Reading, Massachusetts*

21 September 2001 and 1 April 2002

### ABSTRACT

The Geodetic Satellite (Geosat) Follow-On (GFO), Ocean Topography Experiment (TOPEX), and Poseidon altimeter white-noise levels have been evaluated using a technique based on high-pass filtering of 1-Hz sea surface height time series. High-pass filtering removes the geoid and oceanography signals while revealing the random noise. This filtering technique is simpler to use than the repeat-track method, gives essentially the same results, and makes it easier to analyze much larger amounts of data to investigate subtle variations in noise levels. The new noise-level measurements provided here all show stable noise-process characteristics from cycle to cycle, with a linear dependence of the noise level upon significant wave height (SWH). The GFO altimeter noise level is estimated to be 2.5 cm for an SWH of 2 m. The Poseidon noise level is estimated at 2.0 cm for the same value of 2 m SWH. The TOPEX altimeter noise level is 1.8 cm when the dual-frequency ionospheric correction is included; when this noisy correction is not used, the level is reduced to 1.5 cm. Although the dual-frequency ionospheric correction provides an average improvement over the “Doppler orbitography and radiopositioning integrated by satellite” (DORIS) correction, high-frequency noise enters into the dual-frequency correction via noise from the Ku- and C-band ranges. Because the variations in ionospheric refraction are a relatively long wavelength global effect (with strong dependence on latitude), the dual-frequency ionospheric correction should be low-pass filtered before use, and this correction should not be included when estimating the high-frequency noise level of the altimeter.

### 1. Introduction

The Geodetic Satellite (Geosat) Follow-On (GFO) and the Ocean Topography Experiment (TOPEX)/Poseidon (T/P) missions are dedicated to the observation of the ocean surface topography from orbit using satellite-based nadir-pointing radar altimeters. The basic data are altimeter-derived sea surface heights (SSH) that are obtained by taking the difference of the satellite altitude (relative to a reference ellipsoid) as determined by precision orbit tracking and the altimeter range as determined by precise measurement of the round-trip time of flight of the radar signal. The range estimate requires environmental corrections, for example, for atmospheric propagation delays and sea-state biases. Measurements of the range in 1-s averages are generally analyzed in applications of altimeter data.

An integral part of the analysis of altimeter datasets is a quantitative evaluation of altimeter instrument noise. This is necessary for monitoring improvements in measurement systems, for projecting future capabilities, and for properly analyzing the data in oceanographic and geodetic applications. The precision of satellite radar altimeter instruments has improved since the earlier programs [the *Geodynamics Experimental Ocean Satellite (GEOS-3)*, Seasat, and Geosat], and continuous improvements in environmental corrections (orbits, ionospheric refraction, tides, etc.) have resulted in modern altimeters (e.g., TOPEX) having absolute errors of only a few centimeters.



The largest contributions to the measured sea surface topography come from 1) geoid undulations, 2) dynamic oceanography associated with geostrophic surface currents and eddies, 3) tides, 4) the sea surface response to atmospheric pressure loading, and 5) altimeter instrument noise; not included in this list are orbit errors, which are very long in wavelength and relatively small in amplitude and which may be ignored for the purpose of this discussion. The elevation variability of the geoid signal is on the order of meters to tens of meters; the oceanographic signals are from a few centimeters to no more than 2 m; and tides in the open ocean are generally less than 1 m but can be predicted by numerical models to better than a few centimeters. The atmospheric loading or “inverse barometer” effect is a few centimeters, and the instrument noise is also at the few-centimeter level. One additional, but small, effect comes from ocean waves and swell. Although very obvious to mariners, waves are not a major factor in the measured sea surface topography, because each altimeter pulse illuminates a circular area on the ocean that is several kilometers in diameter, so the local waves are approximately averaged out. Actually, the averaging out is not perfect, and there is an “electromagnetic bias” correction proportional to significant wave height (SWH) and wind speed that should be made for the most precise uses of altimeter data (e.g., Gaspar et al. 1994).

The original analyses of satellite altimeter noise were developed in the context of geodesy, and “noise” was defined as any effect in the data other than the geoid signal. Noise was studied by comparing the repeatability of the data observed along colinear or repeat tracks. By differencing the data series along two repeat tracks (having a cross-track offset of no more than 1 km), the time-invariant geoid signal cancels out and a time series of random noise remains. Spectral analysis of the difference time series reveals two main components of the noise: 1) a “colored” noise process behaving approximately like a first-order Markov random process (this is attributable to oceanography) and 2) a lower-powered additive contribution that appears as a “white-noise floor,” visible as the noise spectra flatten out at high frequency (Brammer and Sailor 1980; LeSchack and Sailor 1988). The white-noise component was attributed to electronic noise in the altimeter instrument, and, indeed, the on-orbit results are generally consistent with laboratory measurements of instrument noise made before launch.

However, as this paper shows, a portion of the white-noise component can be attributed to random scattering effects from ocean waves, since the white-noise level is found to be proportional to the SWH. The repeat-track method of studying noise in altimeter data requires that repeat tracks be matched up and aligned, that environmental corrections (e.g., tides) be applied independently to each track, and that power spectra be computed from the difference segments. This is straightforward but was not easily automated to process large amounts of data. Consequently, the early studies did not apply this method to very many repeat-track pairs and did not investigate in much detail the variability in noise

that might occur as a function of aging of the spacecraft or that might be due to environmental factors such as SWH. Nevertheless, the white-noise level for each altimeter was found to be fairly consistent, and the average values obtained for different altimeters are a good measure of the relative quality of those instruments. For example, *GEOS-3*, launched in 1975, had a white-noise level of about 23 cm. For *Seasat* in 1978 the result is 5 cm, and for *Geosat* in 1985 it was 3 cm (Sailor and LeSchack 1987; Sailor and Driscoll 1992). Le Traon et al. (1994) analyzed TOPEX and Poseidon spectra and estimated that the Poseidon repeat-track noise level is about 3 cm and the TOPEX repeat-track noise level is about 1.8 cm, calculated as rms. All of these numbers have been determined without consideration of the SWH. They all represent the integrated white-noise power in the frequency band from  $-0.5$  to  $+0.5$  Hz (the folding frequencies for data sampled at 1 Hz), so these noise values correspond to a 1-s average. Sailor (1993) defines the signal processing and spectral analysis techniques in detail and gives examples that confirm the validity of the noise-modeling approach that involves repeat tracks.

To summarize and conclude, the assessment of the altimeter noise by high-pass filtering 1-Hz sea surface height time series can be applied to single-frequency altimeter data such as from GFO and the French altimeter Poseidon, as well as to dual-frequency altimeter data such as from TOPEX. As pointed out in an early analysis (Driscoll and Sailor 2001), this approach to estimating the altimeter noise provides results similar to those derived from the noise spectra computed from differenced repeating ground tracks and is also in agreement with the alternate operational TOPEX Ku-band range noise estimation method as presented in this paper.

This paper presents the first application of the high-pass-filtering method to multiple altimeters for determining the noise level in satellite altimeter data. This technique is found to be valuable because it allows the noise levels to be determined from individual tracks rather than from repeat tracks, facilitating time-dependent noise-level monitoring. The most obvious effect on the observed noise level is SWH, and, for all altimeters, the noise level increases linearly with increasing SWH. Other than the dependence on SWH, the noise level is very stable from cycle to cycle for GFO, TOPEX, and Poseidon. Thus, the high-pass-filtering technique will be useful for monitoring the performance of any altimeter as the satellite ages and for comparing the relative performance of different altimeters with respect to high-frequency noise.

As shown here, the effective number of independent radar return pulses directly affects altimeter range estimation precision. The new Poseidon-2 altimeters aboard the *Jason-1* satellite transmit at rates of 1800 and 300 Hz, for Ku and C band, respectively. Altimeters aboard *Envisat* operate at 1800 Hz at Ku band and 450 Hz at S band. These rates will thus set limits for both sensor's performance, as pointed out by Quartly et al. (2001).

## The Dependence of Nadir Ocean Surface Emissivity on Wind Vector as Measured With Microwave Radiometer

Ngan Tran, Douglas Vandemark, Christopher S. Ruf, and  
Bertrand Chapron

**Abstract**—Global brightness temperature observations of TOPEX/Poseidon microwave radiometer (TMR) at 18, 21, and 37 GHz have been collocated with near-simultaneous SeaWinds wind vector data as well as with monthly sea surface temperature and salinity products. The combined data allow us to study the dependence of zenith-directed ocean surface emissivity, at each frequency, upon both wind speed and direction. Results show a clear two-branch wind speed dependence; weak and linear below  $7 \text{ m}\cdot\text{s}^{-1}$  with an increase in sensitivity above that point. The observed emissivity also depends on the angle between the wind direction and TMR's antenna polarization orientation, providing satellite confirmation of aircraft-derived results. There is little change in these wind vector dependencies with frequency.

**Index Terms**—Nadir ocean surface emissivity, SeaWinds wind vector, TOPEX/Poseidon microwave radiometer (TMR).

### I. INTRODUCTION

The TOPEX/Poseidon microwave radiometer (TMR) is a three-frequency radiometer operating on the TOPEX/Poseidon (T/P) satellite. It measures radiometric brightness at 18, 21, and 37 GHz in a nadir-viewing direction co-aligned with T/P radar altimeters [1]. Its primary objective is to monitor and correct for the propagation path delay of the Ku-band altimeter signal due to atmospheric water vapor and cloud liquid water [2]. For TMR, this wet tropospheric path delay is derived from the three-frequency brightness temperatures  $T_b$  as discussed in [3]. Delay is highly variable in space and time and, if uncorrected, leads to altimeter range measurement errors of 3–45 cm. TMR is designed to provide this range correction with 1.2 cm accuracy.

Most satellite altimeters are now supported by a two- or three-frequency water vapor radiometer. One issue in designing these systems is compensation for the second-order brightness temperature variations associated with changing ocean surface emission. While the wind speed dependence of zenith-directed emission is fairly well known and already characterized within path delay algorithms, it has also been shown [4] that there should be a small  $\Delta T_b$  associated with wind direction change. This sensitivity comes from the fact that the thermal emission from anisotropic sea waves depends upon azimuthal (polarization at nadir) observation angle.

Several experimental studies have addressed this sensitivity to the wind vector by means of circle flights [4]–[8]. These aircraft measurements indicate a direction detection capability for nadir-looking systems as well as a potential error source for spaceborne water vapor radiometers (such as TMR) aboard altimeter platforms. Reported measurements and theoretical investigations [9]–[11] suggest that the nadir-looking radiometer directional sensitivity follows from the azimuthal anisotropy of the spatial spectrum of short-gravity and capillary waves.

The aim of this communication is to use satellite data from the TMR to document the impact of wind speed and direction on surface emissivity at 18, 21, and 37 GHz. To the authors' knowledge, the study presents the first on-orbit evidence of a wind direction dependence at nadir. This work follows similar efforts focused on the off-nadir pointing spaceborne Special Sensor Microwave/Imager (SSM/I) deployed on the Defense Meteorological Satellite Program (DMSP) missions [12], [13]. The approach is simply to observe  $\Delta T_b$  variation versus the angle between TMR's linear polarization alignment and the surface wind direction. To this end, a large global data set has been compiled by combining scatterometer (SeaWinds) wind vector

measurements with T/P observations at satellite crossover points over a year-long period. The extensive data set carries a broad coverage of environmental conditions and permits robust removal of the first-order atmospheric signal needed to isolate the surface emission signals with certainty. In Section II, we recall Giampaolo and Ruf's [14] approach for TMR emissivity estimation using quantities that can either be obtained directly from satellite measurements or approximated from ancillary sources with satisfactory accuracy. Section III describes the large global compilation of TMR, SeaWinds wind vector, the monthly sea surface temperature ( $T_s$ ) climatological estimates, and the climatological sea surface salinity (SSS) product used in this study. Sections IV and V present, respectively, wind speed and wind direction dependencies of the sea surface emissivity as measured with TMR. Section VI provides conclusions.

### VI. CONCLUSION

Observations presented in Sections IV and V serve to document the zenith-directed wind-induced ocean emissivity ( $\Delta\epsilon$ ) at 18, 21, and

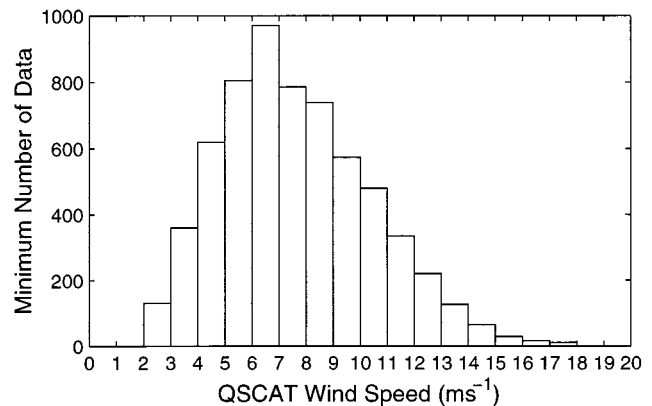


Fig. 7. Minimum number of data in a  $30^\circ$  azimuth angle bin for each  $1 \text{ m}\cdot\text{s}^{-1}$  SeaWinds/QSCAT wind speed interval.

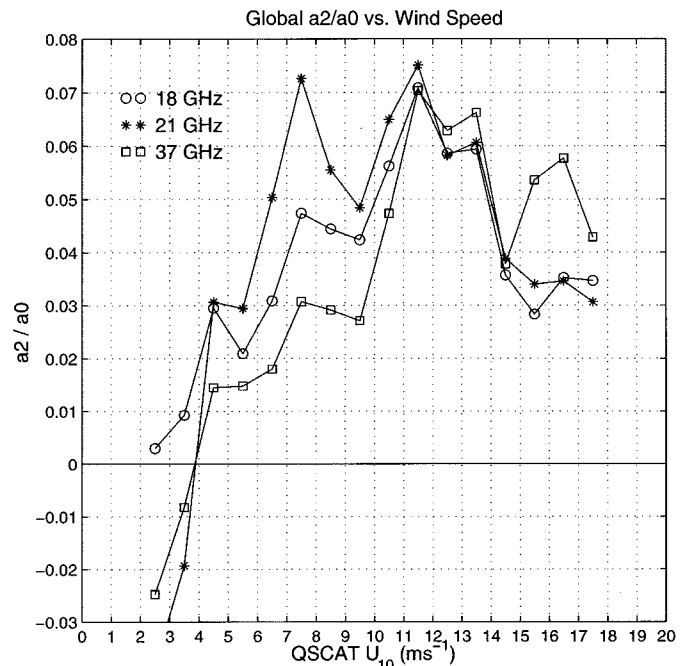


Fig. 8. Dependence of the normalized second-order harmonic  $a_2/a_0$  on SeaWinds/QSCAT wind speed.



37 GHz. These data come from a carefully filtered combination of TOPEX radiometer and SeaWinds scatterometer data, augmented by surface temperature and salinity estimates. The nadir-detected satellite brightness temperature is shown to depend on both wind speed and

direction. This study represents the first satellite confirmation of a directional sensitivity at nadir.

The data show a clear two-branch wind speed dependence; weak and linear below  $7 \text{ m} \cdot \text{s}^{-1}$  with an abrupt increase in sensitivity above that point for all TMR three frequencies. The  $\Delta\epsilon$  is a factor of two to three higher above  $7 \text{ m} \cdot \text{s}^{-1}$ . As mentioned, the microwave emission exhibits a smaller, but measurable, dependence on wind direction. This signal is attributed to the polarized nature of the surface wave structure. The peak-to-peak brightness temperature directional signal is of the order of  $1.0 \text{ K}$  at  $11.5 \text{ m} \cdot \text{s}^{-1}$ . Observations vary little with frequency versus wind speed or direction. These global-average results are the product of a large data compilation and low regression uncertainties. Agreement with previous aircraft and SSM/I studies suggest high confidence in the findings.

These results are applicable in several areas. First, the data confirm the potential for a nadir-viewing wind direction sensor. Such a sensor would necessarily be a polarimetric radiometer in order to isolate the polarized emission from the largely unpolarized background signal. The globally-derived observations should also serve to complement the results derived from aircraft case studies, where all measurements are being assimilated into ocean emission models [8], [34]. Finally, the accuracy of the water vapor radiometer's altimeter path delay correction can be reassessed based on the present observations. As discussed in [35], the two frequency systems are most susceptible to an additional frequency-independent error source (such as  $\Delta\epsilon$  dependence on direction). For example, the GEOSAT-follow-on (GFO) or ERS radiometers operate near 22 and 37 GHz. A first-order estimate suggests that a  $0.20 \text{ cm}$  wet path delay error (and hence sea level error) will result from a peak-to-peak directional  $T_b$  variation of  $1.2 \text{ K}$  at both 22 and 37 GHz. While this level is certainly small, ocean basins can systematically differ in their mean wind directions. Therefore, the error is not necessarily random.

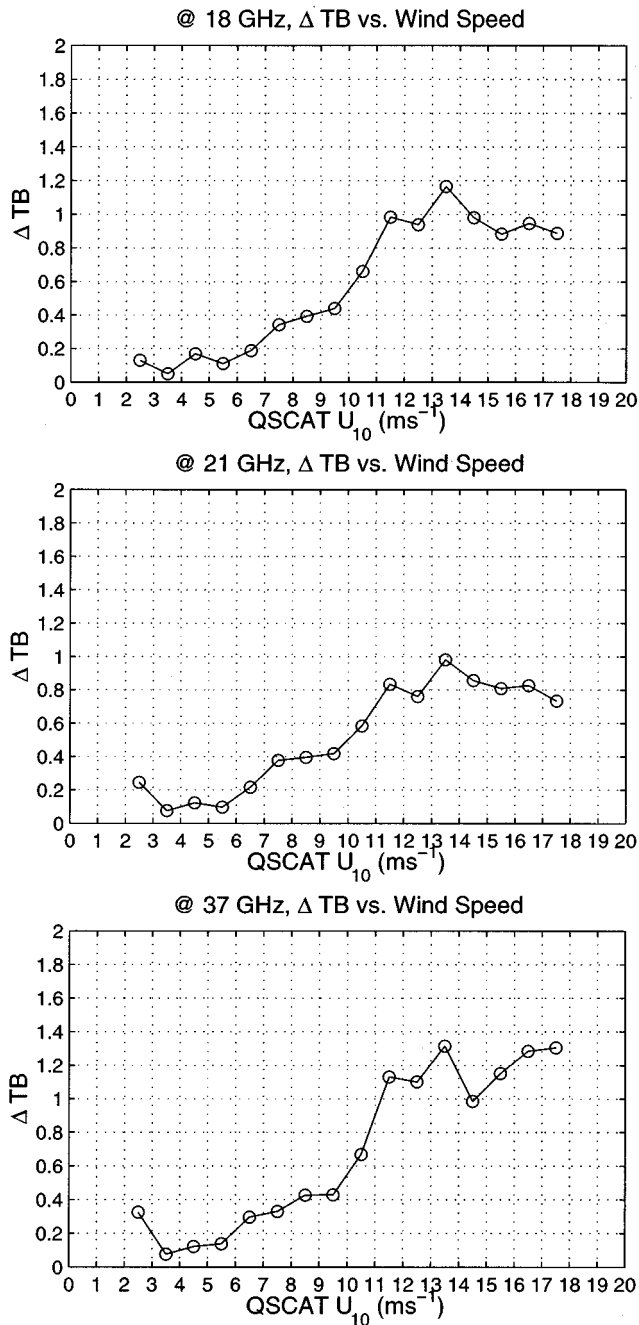


Fig. 9. Amplitude of the directional signal in term of peak-to-peak brightness temperature as a function of SeaWinds/QSCAT wind speed for the three frequencies.

# A Comparison of the MIR-Estimated and Model-Calculated Fresh Water Surface Emissivities at 89, 150, and 220 GHz

James R. Wang, *Senior Member, IEEE*

**Abstract**—The airborne millimeter-wave imaging radiometer (MIR) measurements over three lakes (surface temperature  $\sim 273$  K) in the Midwest region of the USA during February 1997 were used to estimate surface emissivities at 89, 150, and 220 GHz and the results were compared with those calculated from three different dielectric permittivity models for fresh water. The measurements were during clear and dry atmospheric conditions so that the column water vapor could be accurately retrieved and its effect on the MIR measurements predicted. The standard deviations of the estimated emissivities were found to be about 0.003, 0.004, and 0.008 for 89, 150, and 220 GHz, respectively. The errors of the estimation were calculated to be  $\pm 0.005$ ,  $\pm 0.006$ , and  $\pm 0.011$  in the same order of frequency, respectively, based on the MIR measurement accuracy of  $\pm 1$  K in the brightness temperature range of 190–290 K.

The estimated emissivities at normal incidence, under the assumption of a calm water surface, compare quite well with values generated by the model of Stogryn *et al.* [1]. These estimated values are slightly lower than those calculated from the model of Liebe *et al.* [2] at both 89 and 150 GHz. The estimated 89 GHz emissivity is higher than that calculated from the model of Ellison *et al.* [3]. Additionally, the retrievals using different models of atmospheric absorption as well as off-nadir measurements of the MIR are explored. The impact of these retrievals on the comparison of estimated and calculated emissivities is discussed.

**Index Terms**—Millimeter-wave radiometry, remote sensing, surface emissivity.

## I. INTRODUCTION

MICROWAVE remote sensing of atmospheric and oceanic parameters such as water vapor, clouds, precipitation, surface wind and temperature from aircraft and satellite platforms depends crucially on the knowledge of surface emissivity (or reflectivity) and therefore the dielectric permittivity of water. A number of models for the dielectric permittivity of water [1]–[4] have been formulated in the past decades to facilitate measurements of these parameters. At low frequencies  $\leq 10$  GHz, the complex dielectric permittivity,  $\epsilon$ , of water and its temperature dependence appear to comply with Debye's model of single-frequency dielectric relaxation [3]–[5]. In the frequency range below 85 GHz covered by the special sensor microwave/imager (SSM/I) or other satellite radiometers that were used to retrieve parameters like column water vapor clouds, and wind speed over ocean surface [6]–[8], the results of emissivity calculations based on the single-frequency model were not completely satisfactory [8]. Dual-frequency models based on new measurements have been formulated [1], [2], but these models lack extensive testing. More recently, the radiometric measurements at higher frequencies than 85 GHz have been used for studying and retrieving water vapor, clouds, and precipitation [9]–[11]. Thus, it is important to examine the

adequacy of  $\epsilon$  values derived from these models at frequencies  $> 10$  GHz for reliable retrievals of these atmospheric and oceanic parameters.

In this paper, we attempt to validate three recent models of dielectric permittivity for fresh water [1]–[3] from the 89–220 GHz radiometric measurements of the millimeter-wave imaging radiometer (MIR). MIR is a total power, cross-track scanning radiometer that measures radiation at the frequencies of 89, 150,  $183.3 \pm 1$ ,  $183.3 \pm 3$ ,  $183.3 \pm 7$ , and 220 GHz [12]. The measurement accuracy of the instrument is within  $\pm 1$  K in the temperature range of 190–290 K. Racette *et al.* [12] provided a more detailed description of the characteristics and operation of the instrument. For profiling of water vapor using the MIR measurements over a water surface, the surface temperature  $T_s$  and emissivity  $\xi$  calculated from a given dielectric permittivity model are the known parameters that are used as input for a retrieval algorithm [13]. However, when the atmosphere is relatively dry with total column water  $W \leq 0.8$  g/cm<sup>2</sup>, it is possible to estimate  $W$  with good precision, without a detailed knowledge of  $T_s$  and  $\xi$ , from the MIR measurements over a water, sea ice or land surface [14]–[16]. Then  $\xi$  and its frequency dependence are readily determined after  $W$  is estimated and  $T_s$  is independently measured. This procedure is explored in an effort to estimate  $\xi$  of a water surface at 89, 150, and 220 GHz. Estimation of both  $W$  and  $\xi$  from the MIR measurements depends on the selection of atmospheric absorption models; therefore, a brief discussion of the models of atmospheric absorption and water's dielectric permittivity is given in the next section. This is followed by a description of the MIR measurements and retrievals of  $W$  and  $\xi$ . Finally, a comparison between the estimated and calculated  $\xi$  values as well as the ensuing discussion and conclusion of the results are presented.

## II. MODELS OF ATMOSPHERIC ABSORPTION AND DIELECTRIC PERMITTIVITY FOR WATER

### A. Atmospheric Absorption

The millimeter-wave propagation model (MPM) formulated by Liebe [17] is frequently used in radiative transfer calculations, in the microwave-millimeter-wave region of the electromagnetic spectrum, in recent years [13], [18]–[20]. More recently, Rosenkranz [21] reexamined most of the available data and formulated a new model, which was used by Westwater *et al.* [20] to compute  $T_b$  values from rawinsonde data acquired at Barrow, Alaska and compared with near concurrent measurements from ground-based radiometers during March 1999. Westwater *et al.* [20] found subtle differences between the cal-

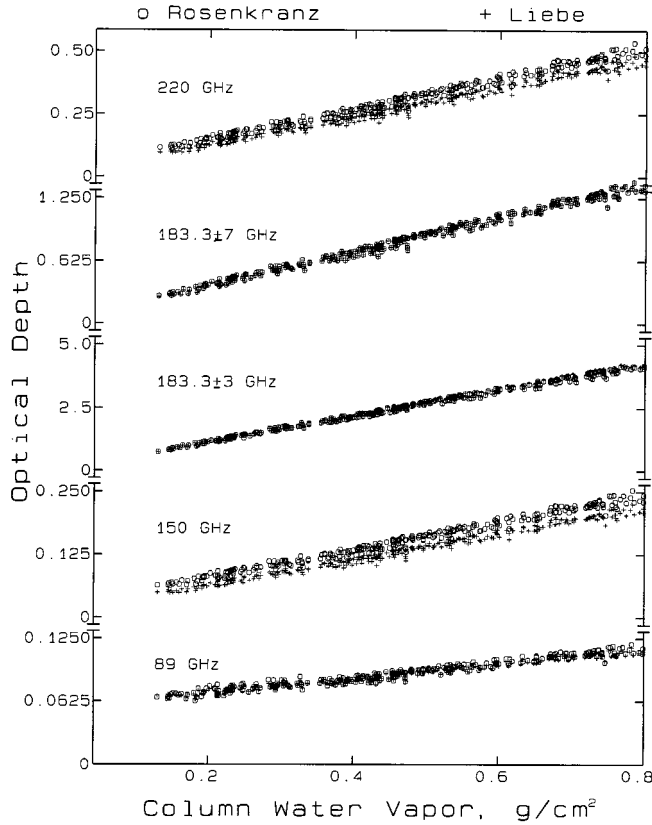


Fig. 1. Scatter plot showing the dependence of optical depth on column water vapor for several selected MIR channels. The values of optical depth are calculated based on the rawinsonde data from the Midwest USA and Alaska-Arctic regions [15].

culated and measured  $T_b$  values, as well as the calculated values between the models of Liebe and Rosenkranz. To see the differences in the MIR frequency range between these two models under dry atmospheric conditions with  $W \leq 0.8 \text{ g/cm}^2$ , we show in Figs. 1 and 2, respectively, the calculated optical depth  $\Gamma$  and  $T_b$  based on rawinsonde data used by Wang *et al.* [15], [16] from both WINCE and FIRE-ACE. The vertical scales from both figures are adjusted in an effort to distinctively demonstrate the variations of  $\Gamma$  and  $T_b$  at each frequency. In the  $T_b$  calculations, the dielectric permittivity model by Stogryn *et al.* [1] for fresh water is used to derive surface emissivity, assuming a water temperature of 274 K.

## VII. CONCLUSION

The MIR measurements over Lake Huron, Lake Michigan, and Lake Superior under clear and dry atmospheric conditions were used to estimate surface emissivity  $\xi(\nu)$  of fresh water. The estimated  $\xi(\nu)$  values at  $\nu = 89, 150$ , and 220 GHz were compared with those calculated from three different models of dielectric permittivity [1]–[3]. Both along-track and across-track measurements were used; thus, the retrieved column water vapor  $W$  and  $\xi(\nu)$  could be analyzed with respect to incidence angle ( $\theta$ ) up to  $40^\circ$ . The retrieved  $W$  values depend on  $\theta$  as expected from a path length consideration. A positive gradient in  $W$  from southeast to northwest of Lake Huron during the time of the aircraft flight is revealed by the retrieval. The  $\theta$  dependence of the retrieved  $\xi(\nu)$  follows

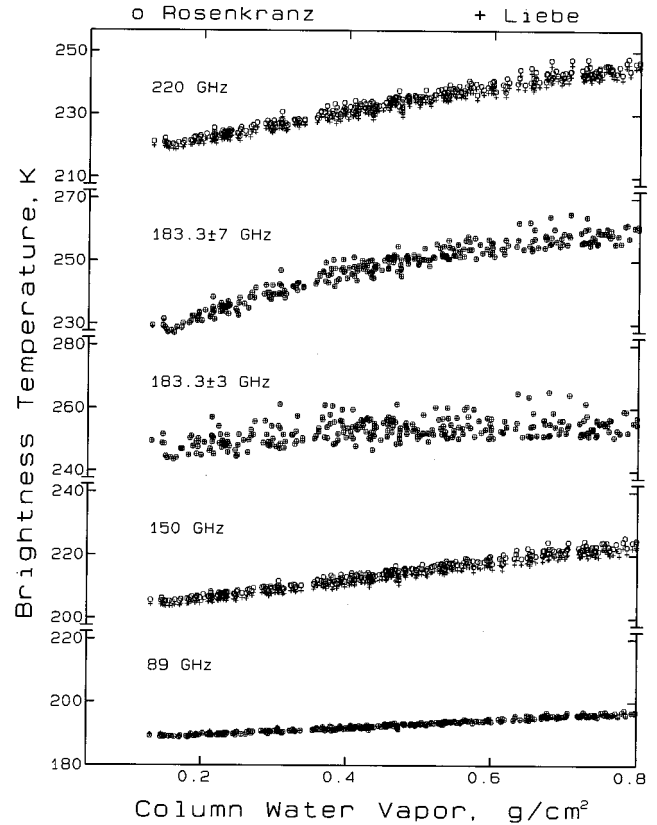


Fig. 2. Scatter plot showing the dependence of brightness temperature on column water vapor for several selected MIR channels. The calculations are based on the same rawinsonde data as in Fig. 1.

a pattern expected from the polarization vector of the MIR. The standard deviations of the retrieved  $\xi(\nu)$  values and their frequency dependence are consistent with those estimated from statistical considerations.

The  $\xi(\nu)$  values retrieved at 89, 150, and 220 GHz for fresh water are in good agreement with those calculated from the dielectric permittivity model of Stogryn *et al.* [1] in the limited temperature range near 273 K, especially if the Liebe's MPM model is used to account for the effect of atmospheric absorption [17]. When Rosenkranz's atmospheric model [21] is used the estimated  $\xi(\nu)$  at 150 GHz appears low compared to all model calculations. The dielectric permittivity model of Liebe *et al.* [2] gives  $\xi(\nu)$  values at both 89 and 150 GHz, which are slightly higher than the estimated values (i.e., just outside of errors based on  $\pm 1 \text{ K}$  measurement accuracy of the MIR). Finally, the estimated  $\xi(\nu)$  values at 89 GHz are about 0.012 higher than those calculated at  $T_s = 273 \text{ K}$  from the model of Ellison *et al.* [3] for seawater. Because the  $\xi(\nu)$  values for fresh water are generally lower than those of saline water, this difference suggests a lower bound of the disagreement between estimation and calculation, unless the enhanced  $\xi(89)$  can be totally accounted for by a wind-roughened surface effect. The  $\xi(89)$  curve calculated from the model of Ellison *et al.* displays a milder dependence on  $T_s$  than those calculated from the other three models. It will be interesting to examine the  $T_s$  dependence of  $\xi(\nu)$  and, therefore, the complex dielectric permittivity over a wider  $T_s$  range than available from the data used in this paper.

# Profiling of Atmospheric Water Vapor With MIR and LASE

James R. Wang, *Senior Member, IEEE*, Paul Racette, *Member, IEEE*, M. E. Triesky, E. V. Browell, S. Ismail, and L. A. Chang

**Abstract**—Concurrent measurements of atmospheric water vapor profiles were conducted over the Atlantic Ocean on September 25, 1995 with both the millimeter-wave imaging radiometer (MIR) and lidar atmospheric sounding experiment (LASE) on board the NASA ER-2 aircraft. LASE provides high precision measurements of both aerosol backscatter and water vapor profiles; aerosol backscatter has a vertical resolution of 60 m while the water vapor profiles have a resolution of 330 m in the low-to-mid troposphere and 550 m in the upper troposphere. Therefore, LASE measurements provide an excellent resource for assessing the capabilities and limitations of MIR as a water vapor profiler. Previously, the water vapor profiles retrieved from the MIR measurements have been compared with those of rawinsonde and Raman lidar observations at point locations. The frequency and extent of the comparisons made in that fashion were largely constrained by the requirement of near coincidence in time and space. The data acquired concurrently by MIR and LASE from this ER-2 aircraft flight enable the comparison of MIR-retrieved and LASE-measured moisture profiles over a long stretch of time and space. In addition, the LASE-measured profiles of aerosol backscatter provide a resource to assess the impact of clouds on the retrieval of water vapor profiles from the MIR measurements.

It is shown that profiles of water vapor mixing ratio retrieved from the MIR data generally conform to those measured by the LASE; however, differences in the values of mixing ratio at individual altitude levels are quite often not small. The standard deviations of these differences are found to be about  $\pm 0.98$ ,  $\pm 0.84$ ,  $\pm 0.95$ ,  $\pm 0.42$ , and  $\pm 0.06$  g/kg at altitudes of 1.25, 2.75, 4.75, 7.25, and 10.25 km. It is demonstrated that a substantial portion of these differences are due to the poor vertical resolution inherent in the profile retrieval using the MIR radiometric measurements. Additionally, MIR water vapor profiling under cloudy conditions is demonstrated, and it is shown that location and height of the low-altitude clouds estimated from the retrieval process were generally consistent with those observed by the LASE. For study cases where cirrus clouds are present, retrievals from the MIR data over-estimate the mixing ratio; this over-estimate is provoked by brightness temperature decreases that occur at 183–220 GHz within these regions. Undoubtedly, the retrieval method needs an additional procedure to account for the millimeter-wave scattering by cloud ice particles so that water vapor profiling can be improved within regions where cirrus clouds are present.

## I. INTRODUCTION

**P**ROFILING of atmospheric water vapor using the strong absorption line at 183.3 GHz has been studied for nearly two decades [1]–[13]. Theoretically, Schaerer and Wilheit [1] explored the characteristics of this strong water vapor line by performing both forward calculations and profile retrievals over the ocean surface. The approach was extended by Wilheit [7] to retrieve water vapor profiles under both clear and cloudy conditions. Other alternative simulation studies and analyses have been performed by Rosenkranz *et al.* [2], Kuo *et al.* [11] and Muller *et al.* [12]. Experimentally, water vapor

**Index Terms**—Millimeter-wave radiometry, remote sensing, water vapor.

profiles have been retrieved using radiometric measurements by the Airborne Microwave Moisture Sounder (AMMS) in the 1980s [3]–[6]. Because of its limited number of channels and poor temperature sensitivity ( $\Delta T$ ), the AMMS radiometric measurements could not provide robust retrievals of water vapor profiles under cloudy conditions [8]. More recently, a millimeter-wave imaging radiometer (MIR) was built and after a number of field experiments [9], [10] the radiometer was shown to provide more robust radiometric measurements than the AMMS. It contains six channels in the frequency range of 89–220 GHz and, with a comparable integration time to the AMMS, has  $\Delta T$ 's of  $<1$  K at all channels [14]. The radiometric measurements from this sensor have been used to retrieve water vapor profiles under cloudy conditions with reasonable success [10]. Burns *et al.* [13] have also examined the effects of precipitation and cloud ice on these water vapor channels using measurements from the special sensor microwave/temperature-2 (SSM/T-2) on board the defense meteorological satellite program (DMSP) F-11 satellite. These theoretical and experimental efforts provide an effective demonstration of the capabilities and limitations of using the 183.3 GHz line for water vapor profiling.

The experimental results of water vapor profiling derived from the AMMS and MIR measurements were routinely compared with nearly concurrent (within  $\pm 3$  hours) rawinsonde observations at some selected locations [3], [6], [9]. Additionally, a comparison of water vapor profiles retrieved from the MIR measurements was made with ground-based Raman lidar observations at NASA's Wallops Flight Facility (WFF), Wallops Island, Virginia during the Convection and Atmospheric Moisture Experiment (CAMEX) of July–August, 1993 [9]. Reasonable agreements were found between the profiles retrieved from these AMMS and MIR measurements and those measured at the ground locations. However, these comparisons were limited to single locations and there has been no validation of the profiles retrieved from the measurements of these sounders over an extended region. During September 1995, MIR and LASE (Lidar Atmospheric Sensing Experiment) were on board the NASA ER-2 aircraft during a number of flights both over land and ocean areas in the eastern U.S. LASE measures both aerosol backscatter and water vapor mixing ratio with high accuracy and vertical resolution [15], [16]. The LASE-measured mixing ratio was compared with that measured concurrently by the ground-base Raman Lidar

and rawinsondes at WFF and an excellent agreement was found among the three different approaches [15]. These flights provide the first opportunity to validate the water vapor profiling method derived from the MIR radiometric measurements over an extended region.

## VI. CONCLUSION

Measurements of water vapor profiles were made concurrently with LASE and MIR on board the NASA ER-2 aircraft over the Atlantic ocean on September 25, 1995. The LASE measured profiles have a vertical resolution of 330 to 550 m, depending on altitude, and, therefore, serve as an excellent standard for comparison with the lower-resolution profiles retrieved from the MIR measurements. Previously, the water vapor profiles obtained from the MIR measurements were compared only with those measured by dropsondes released from a different aircraft or by the ground-based Raman lidar and rawinsondes [9], [10]. The requirement of the approximate coincidence in time and location of these measurements essentially limited the comparison to a few selected cases. The 3-h flight of LASE and MIR described above, on the other hand, provides about 180 independent and concurrent measurements over an ocean area that includes both clear and cloudy conditions. This combined LASE and MIR data set serves as an extremely valuable resource that can be utilized to analyze and evaluate the capabilities and limitations of millimeter-wave remote sensing to profile water vapor. However, there is a deficiency related to this data set: it is obtained within a short time period over a small geographic region and, as a consequence, the range of observed variation in the moisture field of the atmosphere is rather limited.

The comparison of the MIR-retrieved profiles of water vapor mixing ratio with those measured by LASE leads to the following conclusions. First, in general the MIR-retrieved profiles correspond well with those measured by the LASE, although they could not provide the fine vertical structure reflecting the rapid changes of moisture with altitude that was observed by LASE. At individual altitude levels, the differences in the mixing ratios retrieved by the MIR and measured by LASE are not small. A substantial portion of these differences is undoubtedly caused by the poor vertical resolution of the retrieved profiles that is inherent to the inversion process. For instance, column 3 of Table I shows that, using LASE measurements as a standard, the inversion process could cause standard deviations of  $\pm 0.95$ ,  $\pm 0.57$ ,  $\pm 0.16$ , and  $\pm 0.02$  g/kg at the altitudes of 2.75, 4.75, 7.25, and 10.25 km. The retrieval results from the MIR measurements give corresponding numbers of  $\pm 0.84$ ,  $\pm 0.95$ ,  $\pm 0.42$ , and  $\pm 0.06$  g/kg at those respective altitudes; the larger numerical values at higher altitudes could be attributed to the measurement differences between the two sensors. The standard deviations were significantly smaller than those of climatological variations. Therefore, radiometric measurements at the MIR frequencies can provide water vapor profiles that are useful

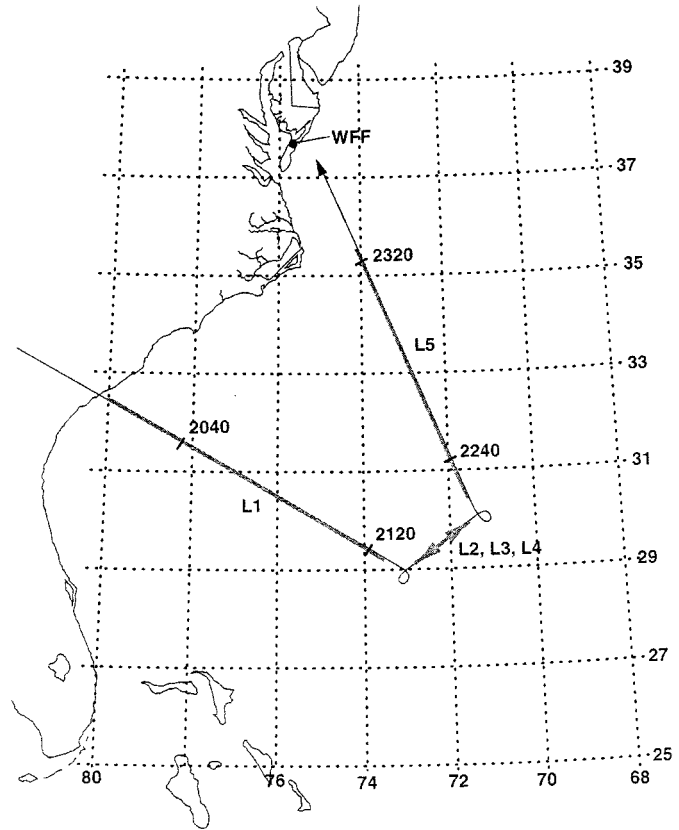


Fig. 1. Sketch showing the path of the ER-2 aircraft flight over the Atlantic Ocean on September 25, 1995. Five straight line segments are denoted by L1, L2, L3, L4, and L5. L2, L3, and L4 are repeated passes over the same region.

for studying the large-scale changes in the water vapor fields of the atmosphere.

Next, it was shown that MIR could profile atmospheric water vapor over a region with moderate, low-altitude cloud cover. There is a close association between the locations where low-level clouds are detected by LASE and the locations where the cloud liquid water were also required as input to the MIR retrieval algorithm to reach a convergent retrieval of water vapor profiles from the MIR measurements. The cloud tops predicted by the retrieval algorithm are closely related to those observed by the LASE; however, the retrieval does experience some difficulty in areas of dense clouds where the measured 89 GHz brightness temperatures are  $>270$  K (Fig. 3). The retrievals for these areas result in low values of mixing ratio at altitudes below the cloud tops, require cloud liquid water in excess of  $0.4$  kg/m<sup>2</sup>, and are associated with poor convergent criteria ( $\Delta T_b \approx 2$ – $3$  K) (see Fig. 4).

Finally, in the region of dense cirrus clouds where the depressions in 220 GHz brightness temperatures are clearly observed, the effect of millimeter-wave scattering by ice particles must be considered to improve retrievals of water vapor profiles. The algorithm used to retrieve water vapor profiles from the MIR measurements, as discussed above, does not currently incorporate such a procedure.

# Retrievals of Column Water Vapor Using Millimeter-Wave Radiometric Measurements

James R. Wang, *Senior Member, IEEE*, Paul Racette, *Member, IEEE*, M. E. Triesky, and Will Manning

**Abstract**—The airborne millimeter-wave imaging radiometer (MIR) measurements conducted over the midwest region of the continental United States during January/February 1997 and over the Alaska–Arctic region during May 1998 are used to estimate column water vapor  $W < 0.8 \text{ g/cm}^2$  under a clear sky. On board the same aircraft are two other instruments, the cloud lidar system (CLS) and MODerate-resolution imaging spectrometer (MODIS) airborne simulator (MAS), which provide cloud cover information and independent measurements of  $W$ , respectively. The MIR-estimated  $W$  values are compared and found to be in very good agreement with those measured by rawinsondes at near concurrence. A close correlation is found between the MIR-estimated  $W$  and that estimated from the MAS near-IR reflectance ratios. Water surface emissivities at several MIR frequencies are obtained in the process of the  $W$  retrieval from several flights over the mid-west lakes. These estimated emissivities compared favorably with values calculated for a calm water surface, which are based on a recent dielectric permittivity model and MAS-measured surface temperatures. The results from all comparisons strongly demonstrate the soundness of the technique for estimating  $W$ .

**Index Terms**—Millimeter-wave radiometry, remote sensing, water vapor.

## I. INTRODUCTION

MILLIMETER-WAVE radiometry with the strong absorption line of 183 GHz is normally used for profiling of water vapor, as both theoretical and experimental studies have demonstrated during the past two decades [1]–[5]. Additionally, some studies have shown that measurements near this line can be used to estimate total amount of water vapor column  $W$  for relatively dry atmospheric conditions that frequently occur in high latitude regions [6] or following a cold air outbreak [7]. Over Antarctica or the arctic region, dry-air conditions are prevalent from late fall to early spring so radiometry near 183 GHz provides an excellent resource for  $W$  estimation. Monitoring the state of atmospheric water vapor and its transport into and out of these regions is important toward our understanding the state of balance of ice sheets and its effect on global sea level [8]. Both Moore [9] and Miao [10] have selected Antarctica as their study area for estimation of  $W$  from measurements of the 183 GHz channels of the special sensor microwave/temperature-2 (SSM/T-2); however, the techniques employed by these authors are different. Moore [9] used measurements from the  $183.3 \pm 3$  and  $183.3 \pm 7$  GHz channels of the SSM/T-2, as well as the surface temperature derived from the European Center for Medium-range Weather Forecast (ECMWF) data source to simultaneously retrieve both  $W$  and surface reflectivity,  $R$ , using an iterative technique. Miao [10], on the other hand, used a regression approach with the SSM/T-2 measurements at 150,  $183.3 \pm 3$ , and  $183.3 \pm 7$  GHz as inputs.  $R$  is assumed constant over the frequency range of 150–183 GHz in the latter approach.

Wang *et al.* [11] attempted to apply these techniques of Moore [9] and Miao [10] for estimation of  $W$  while using airborne MIR (Millimeter-wave Imaging Radiometer) measurements over Alaska and Arctic region on May 20, 1998 instead of the SSM/T-2 data. The flight is one of many conducted during the FIRE-ACE (First ISCCP (International Satellite Cloud Climatology Project) Regional Experiment—Arctic Cloud Experiment) field campaign that occurred from May 18–June 6, 1998. However, the thermal IR channels of the MODIS (MODerate-resolution imaging spectrometer) airborne simulator (MAS) on board the same NASA ER-2 aircraft were not functioning properly during that clear day of flight and, thus, the analysis was limited to the technique of Miao [10]. In addition to the data from the frequency group of  $150, 183.3 \pm 3$ , and  $183.3 \pm 7$  GHz that is needed for estimation of  $W$ , MIR also provided measurements at 220 GHz; therefore,  $W$  can be estimated independently using data from the frequency group of 220,  $183.3 \pm 3$ , and  $183.3 \pm 7$  GHz. The results from both frequency groups can then be compared. Wang *et al.* [11] analyzed the MIR data from both frequency groups and found discrepancies of various amounts in the estimated  $W$  values. They attributed these discrepancies to the unsubstantiated assumption that  $R$  (or emissivity  $e$ ) is constant across the frequency ranges of 150–183 GHz and 183–220 GHz. They modified the technique by allowing a linear dependence of  $e$  on frequency over the entire frequency range of 150–220 GHz; by varying the slope of this linear dependence, estimated  $W$ s were forced to converge to a common value. The results obtained from this modified version of the technique appeared reasonable. The estimated  $W$  values were compared with the available rawinsonde data at two locations and the differences between the estimated and measured  $W$  values were within the accuracy of the radiometric measurements. A more extensive comparison with rawinsonde data was not possible, because all other flights from that mission were made when atmospheric conditions were too moist for the retrieval technique to be applicable.

In the following we extend the previous work of Wang *et al.* [11] to the MIR data obtained from the flights over the Midwest region of the continental U.S. during the WINTER cloud experiment (WINCE) [12] of January/February 1997. The techniques of both Moore [9] and Miao [10] and its modified version are described and analyzed with simulated brightness temperatures from a vast number of rawinsonde data from the Alaskan, Arctic, and Midwest regions. The technique of Moore [9] is proven inadequate for application to the MIR data. The modified version of Miao's technique [11] is used exclusively to estimate  $W$  from the MIR measurements. The estimated  $W$  values from both FIRE-ACE and WINCE are compared with those derived from rawinsonde observations. Additionally, a comparison



is made between these MIR-estimated  $W$ s and those expected from the reflectance ratios in the near IR channels of the MAS. Finally, surface emissivities at several frequencies are estimated from a few observations over the lakes in the Midwest and compared with the calculated results, which substantiate the robustness of the retrieval technique.

## V. CONCLUSIONS

Two different techniques [9], [10] developed recently for the estimation of integrated water vapor  $W < 0.8 \text{ g/cm}^2$  have been examined in this paper. The technique by Moore [9] utilizes the  $183.3 \pm 3$  and  $183.3 \pm 7 \text{ GHz}$  channels of the SSM/T-2 and ECMWF-derived surface temperature to estimate  $W$  and surface reflectivity  $R$  iteratively. Additionally, this approach requires as input an *a priori* optical-depth weighted effective atmospheric temperature in the equations for estimation of  $W$  and  $R$ . This latter requirement is found impractical for the data sets we obtained from the aircraft flights and therefore the technique is not explored further in the paper. The technique of Miao [10] is regression-based and uses the 150,  $183.3 \pm 3$ , and  $183 \pm 7 \text{ GHz}$  channels of the SSM/T-2 to estimate  $W$  over Antarctica. Equivalent surface emissivity values in the frequency range of 150–183 GHz are assumed in this approach, which, if not correct, could result in a significant error in the estimation of  $W$  [11]. MIR has an additional channel at 220 GHz that is absent from the SSM/T-2 and thus is capable of providing estimation of  $W$  with a simple linear dependence of  $e$  on frequency in the range of 150–220 GHz. Wang *et al.* [11] provided a demonstration of this modified version of Miao's technique using data from a clear-sky MIR flight over the Alaska-Arctic region on May 20, 1998. The present analysis extends that work to cover additional measurements over several different areas. Furthermore, the estimated  $W$  values are compared with those derived from the near IR channels of the MAS, as well as from a number of rawinsonde data. Additionally, as a by-product of the retrieval process, the surface emissivities at 89, 150, and 220 GHz for several lakes in the mid-west region of the continental U.S. are estimated and compared with results of calculations based on a recent dielectric permittivity model for fresh water [16].

The estimated  $W$  values are found to compare very well with those measured from the rawinsonde data for about the same time and location. On average the estimated  $W$  is about  $0.02 \text{ g/cm}^2$  higher than the measured ground truth, which falls within the accuracy of the radiometric measurements. An increase of about 2 K in the measured brightness temperature at 150 GHz would offset this small bias [11]. The comparison between the MIR and MAS estimated  $W$  values is not exact because the estimation algorithm based on the reflectance ratios from the available near IR channels of the MAS is optimized for  $W > 1 \text{ g/cm}^2$  [15]. Interestingly, the variation in the scatter plot between the MIR estimated  $W$  and the MAS near IR reflectance ratios definitely show a significant correlation.

The estimated and calculated emissivities for fresh water are compared at three frequencies and over four different measurements. Except for a single case at 220 GHz, the estimated and calculated values agree very well. The small differences in the comparison can be accounted for either by considering measurement errors or inadequacy of extrapolation of the dielectric permittivity model to high frequencies. Together, the comparisons with rawinsonde data, MAS reflectance ratios, and emissivity calculations substantiate the soundness of the present regression approach for  $W$  estimation from the four-channel MIR measurements.

The technique presented here is useful for areas with relatively dry atmosphere conditions such as the Arctic region and Antarctica. However, it cannot be applied to the currently available satellite data, which are limited to three channels at 150,  $183.3 \pm 3$ , and  $183.3 \pm 7 \text{ GHz}$ . Using data from these three channels alone requires an assumption of the same emissivity across the frequency range of 150–183 GHz [10], which could result in a significant error in  $W$  estimation [11]. Perhaps an improved method to better characterize surface type and, therefore, approximate frequency dependence of surface emissivity can be devised to resolve this problem. This is a nontrivial problem that remains to be pursued in future studies.

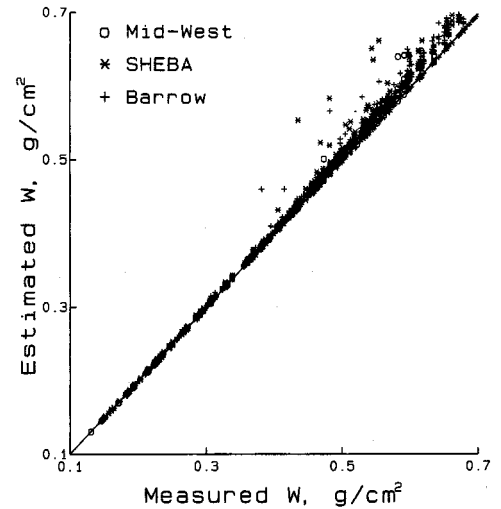


Fig. 1. Scatter plot of  $W$  values estimated from the simulated  $T_b(183.3 \pm 3)$  and  $T_b(183.3 \pm 7)$  and derived from the corresponding rawinsonde from Barrow, Alaska, SHEBA ship, and Mid-West. The surface emissivity is varied between 0.50–0.95 in 0.05 increments in the  $T_b(\nu)$  calculations.

# Autonomous Above-Water Radiance Measurements from an Offshore Platform: A Field Assessment Experiment

G. ZIBORDI

*Space Applications Institute, Joint Research Centre of the European Union, Ispra, Italy*

S. B. HOOKER

*Laboratory for Hydrospheric Processes, NASA GSFC, Greenbelt, Maryland*

J. F. BERTHON AND D. D'ALIMONTE

*Space Applications Institute, Joint Research Centre of the European Union, Ispra, Italy*

(Manuscript received 7 August 2000, in final form 5 June 2001)

## ABSTRACT

An autonomous system for making above-water radiance measurements has been produced by adding a new measurement scenario to a CIMEL CE-318 sun photometer. The new system, called the Sea-viewing Wide Field-of-view Sensor (SeaWiFS) Photometer Revision for Incident Surface Measurement (SeaPRISM), combines the normal CE-318 capability for measuring direct sun irradiance and sky radiance, with a new capability for measuring above-water radiance for the retrieval of water-leaving radiance. The system has been extensively tested during several measurement periods over a 1-yr time frame from August 1999 to July 2000 under various sun elevations along with different atmospheric, seawater, and sea-state conditions. The field assessment of the new instrument was conducted at an oceanographic tower located in the northern Adriatic Sea within the framework of measurement campaigns aimed at supporting ocean color calibration and validation activities. Sample data at 440, 500, 670, 870, and 1020 nm were collected at azimuth and zenith angles satisfying the SeaWiFS Ocean Optics Protocols (and successive revisions) for above-water radiance measurements. Specifically, data were collected with azimuth angles of 90° with respect to the sun plane, and with nadir viewing angles of 30°, 40°, and 45° for above-water measurements and of 150°, 140°, and 135° for sky radiance measurements, respectively (the latter are needed for glint correction of the data). The intercomparison between water-leaving radiances computed from SeaPRISM measurements and those obtained from in-water optical profiles taken with the Wire-Stabilized Profiling Environmental Radiometer (WiSPER) system were performed using 113 coincident sets of measurements collected during clear-sky conditions. The SeaPRISM measurements taken at 40° and corrected for glint effects using different methods show the best agreement with WiSPER data. The intercomparisons exhibit average absolute unbiased percent differences, generally lower than 10% at 440 and 500 nm, and lower than 26% at 670 nm. The intercomparison of the water-leaving radiance ratio  $L_w(440)/L_w(500)$  from SeaPRISM data taken at 40° and WiSPER data exhibits average absolute unbiased percent differences lower than 5.6%.

## 1. Introduction

Water-leaving radiance at wavelength  $\lambda$  in the visible and near-infrared parts of the solar spectrum,  $L_w(\lambda)$ , is the primary parameter for vicariously calibrating ocean color satellite sensors and for validating the algorithms used for estimating chlorophyll *a* concentration (Hooker and McClain 2000). Most spaceborne instruments, like the Sea-viewing Wide Field-of-view Sensor (SeaWiFS), ensure global products on a routine basis, so extensive spatial and temporal measurements of water-leaving radiance are required to satisfy the calibration and validation objectives (McClain et al. 1998).

Oceanographic cruises can ensure the collection of in-water optical profiles over large areas regardless of the water type, but they can only provide data in a restricted time frame (i.e., from days to weeks). Although shading from the deployment platform can be easily avoided through the use of free-falling profilers that can be floated away from the ship, platform stability is still required for solar reference measurements or for water-leaving radiance measurements through above-water methods. The latter feature is particularly important in the coastal environment, because small research vessels are frequently used for nearshore surveys.

In-water moored systems based on buoys, are an alternative platform when the collection of optical data at discrete depths with very good temporal resolution is needed (Clark et al. 1997). The use of moorings is best suited to clear-water regions, so biofouling effects on the submerged optical surfaces are minimized. The negative influence of waves and currents on the pointing stability of the sensors with respect to the vertical, and on the geometric alignment of the sensors with respect to the sun, must be quantified (i.e., the sensors need to be vertically oriented and outside the shadow of the buoy during data collection). Additional difficulty is the extrapolation of the subsurface upward radiance from discrete measurements taken at a few depths. This process can be significantly influenced by different seawater optical properties (e.g., caused by vertical stratification) within the depth intervals defined by the relative locations of each underwater sensor. Taken together, these elements make moored systems a difficult platform for calibration and validation activities in coastal waters, because the biofouling problem is severe, and the sea state and current structure is a strong function of daily and seasonal forcing.

## 5. Summary and conclusions

The intercomparison of SeaPRISM (above-water) and WiSPER (in-water)  $L_w(\lambda)$  data, highlights the difficulty in minimizing glint effects in above-water radiance measurements collected during clear-sky conditions. The methods discussed in this study for the retrieval of  $L_w(\lambda)$  from above-water measurements are based on the removal of sun- and sky-glint effects applying a theoretical sea surface reflectance factor  $\rho(\theta)$  and three different processing schemes: (i) making use of time-averaged data (method S95<sub>a</sub>); (ii) using the minimum value from a sequence of  $L_T(\lambda, \theta, \phi)$  measurements as further minimization of sun-glint effects (method S95<sub>m</sub>); and (iii) using time-averaged data and direct sun irradiance measurements to estimate sun-glint residuals (method S00). Recognizing that the small number of measurements collected during each SeaPRISM sea-viewing measurement sequence (three) reduces the statistical robustness of the  $L_w(\lambda)$  estimates, the intercomparisons nevertheless demonstrate that with  $\phi = \phi_0 + 90^\circ$ , the S95<sub>m</sub> method at  $\theta = 40^\circ$  for spectral averages give the best agreement with WiSPER data.

For the 113 matchups composing the assessment dataset, the S95<sub>m</sub> method exhibits  $|\psi|$  values of 6.1%, 7.1%, and 20.5% at 440, 500, and 670 nm, respectively. The larger  $|\psi|$  values at 670 nm, systematically observed for all the applied processing methods and at all values of  $\theta$ , is justified by the large surface perturbations induced in the above-water measurement in the red part of the spectrum. It is important to remember the data were taken with different solar positions as well as different atmospheric and marine conditions over a 1-yr period—so the variance associated with seasonal forcing is present in the results—but all measurements were made during clear-sky conditions and for wind speed generally less than  $5 \text{ m s}^{-1}$ , that is, in near-ideal conditions. The latter would not be expected for fully operational measurements, and sampling issues raised by other investigators for above-water methods in the coastal environment (e.g., high wind speeds) would have to be considered (Toole et al. 2000).

The intercomparison of radiance ratios  $L_w(440)/L_w(500)$  from SeaPRISM and WiSPER data have  $|\psi|$  values ranging from 4.5% to 5.6% at  $\theta = 40^\circ$ , with the best result derived from the S95<sub>a</sub> and S00 methods. The latter is an important accomplishment, in terms of using SeaPRISM for remote sensing calibration and validation activities, because it is close to the 5% SeaWiFS radiometric objectives. It is important to note the S95<sub>m</sub> method applied for radiance ratios is sufficiently close to the 5% level at  $\theta = 40^\circ$  that additional investigations into the sources of variances might render this method acceptable as well.

The analysis of the uncertainty budget (restricted to instrument overall intercalibration accuracy, tower- and self-shading, and environmental perturbations), shows a quadrature sum of the relative uncertainties generally within 4%–5% for both SeaPRISM and WiSPER radiances, with the exception of the SeaPRISM water-leaving radiance at 670 nm exceeding 12% (Table 4). The latter high value is again justified by the significant contribution of surface effects in the red part of the spectrum

and is in agreement with the data shown in Table 2. This level of uncertainty accounts for approximately half of the spectral differences for the S95<sub>m</sub> method, and it is close to the band ratio differences. The former suggests some additional sources of uncertainty have not been well quantified (e.g., bidirectional effects in the spatial distribution of the in-water radiance field, differences in the above- and in-water tower perturbations, etc.), while the latter suggests that some uncertainties are cancelled or minimized by the band ratio calculation (Hooker et al. 2002).

Based on the results achieved with the SeaPRISM prototype system, the requirements for an operational, fully autonomous system can be considered:

- 1) a maximum number of channels, at the appropriate center wavelengths, for ocean color observations (IOCCG 1998) are needed;
- 2) programmable  $\theta$  and  $\phi$  angles to satisfy the testing or operational use of different measurement protocols;
- 3) the collection of a maximum number of sea-viewing values (per measurement sequence and per channel), to ensure statistical robustness for rejecting measurements contaminated by wave, cloud, and sun-glint effects and to maximize the signal-to-noise ratio;
- 4) characterization of the instrument offset during each measurement sequence; and
- 5) automatic data transmission through a satellite link.

There are a few restrictions with these recommendations if SeaPRISM instruments are to be used within the AERONET activity. First, AERONET requires at least six channels in keeping with WMO recommendations for aerosol and water vapor sun photometry (Frohlich and London 1986), so this leaves two channels for ocean color applications (in addition to the channels within the six for sun photometry that are useful for ocean color work). Given the present form of operational ocean color algorithms (O'Reilly et al. 1998), 443, 490, 510, and 555 nm are appropriate wavelengths to consider. Second, the amount of data that can be transmitted through the satellite link is limited, so to maximize the number of sea-viewing measurements (under most circumstances 11 should be possible), some of the data processing could be handled by the sun photometer control unit. Third, the SeaPRISM system does not include a capability for making  $E_d(0^+, \lambda)$  measurements, which are needed for the computation of normalized water-leaving radiances (Gordon and Clark 1981). For the validation of satellite radiometric data and the vicarious calibration of space sensors; however,  $L_w(\lambda)$  data collected at a time very close to the satellite overpass, may be used without any normalization. Different applications requiring normalized water-leaving radiances could use, during clear sky conditions, the aerosol optical thickness retrieved from the direct sun irradiance measurement and the aerosol scattering phase function derived from the sky radiance measurement as input for a theoretical computation of  $E_d(0^+, \lambda)$ .